

2022-09

Analysis of a Vertical-Axis Tidal Turbine Using the Variational Multiscale Formulation

Dhalwala, Musaddik

Dhalwala, M. (2022). Analysis of a vertical-axis tidal turbine using the variational multiscale formulation (Master's thesis, University of Calgary, Calgary, Canada). Retrieved from <https://prism.ucalgary.ca>.
<http://hdl.handle.net/1880/115327>

Downloaded from PRISM Repository, University of Calgary

UNIVERSITY OF CALGARY

Analysis of a Vertical-Axis Tidal Turbine Using the Variational Multiscale Formulation

by

Musaddik Dhalwala

A THESIS

SUBMITTED TO THE FACULTY OF GRADUATE STUDIES
IN PARTIAL FULFILLMENT OF THE REQUIREMENTS FOR THE
DEGREE OF MASTER OF SCIENCE

GRADUATE PROGRAM IN MECHANICAL ENGINEERING

CALGARY, ALBERTA

SEPTEMBER, 2022

© Musaddik Dhalwala 2022

Abstract

This thesis first investigates the performance and near-wake characteristics of a full-scale vertical-axis tidal turbine under a uniform inflow and turbulent inflow with a 5% and 10% turbulence intensity. The governing equations of the flow field are the incompressible Navier-Stokes equations. As the turbine rotates throughout the simulation, these equations are expressed in a slightly different form referred to as the arbitrary Lagrangian-Eulerian (ALE) framework. The purpose of the ALE framework is to allow the mesh to move arbitrarily while the fluid moves independently of the mesh motion. From the available large eddy simulation (LES) formulations in the literature, the variational multiscale (VMS) formulation is used to discretize the system of equations. Unlike classical LES, the VMS formulation does not have any problems with specifying an appropriate filter for different flows. To study the effect of a turbulent inflow, a turbulence generation method referred to as Smirnov's random flow generation (RFG) is used. From the numerous turbulence generation methods available, Smirnov's RFG was chosen as it can generate a turbulent velocity field that is divergence-free. A divergence-free velocity field ensures compatibility with the incompressible Navier-Stokes equations that govern the flow field and results in good numerical stability.

While the performance of the turbine slightly reduced under a turbulent inflow compared to a uniform inflow, there was a negligible difference in its performance between the two turbulent inflow conditions. A turbulent inflow also resulted in large fluctuations of the instantaneous power coefficient. Lastly, the wake recovery was notably improved under a turbulent inflow. Next, the effect of a free surface on the performance and flow field of the turbine with different blade-strut configurations is studied. There was a negligible effect of the free surface on turbine performance and the flow field during deep immersion. Moreover, the tip-struts configuration was 15% more efficient than the quarter-struts configuration under deep immersion. Under shallow immersion, the performance of both blade-strut configurations reduced.

Preface

This thesis is composed of the following publications: [Dhalwala et al. \(2022\)](#) and [Bayram et al. \(2022\)](#). The following are taken from [Dhalwala et al. \(2022\)](#): Sections 1.1, 1.2, 1.5, and 5.1; Chapters 2 and 3. The following are taken from [Bayram et al. \(2022\)](#): Sections 1.3 and 5.2; Chapter 4. Musaddik Dhalwala wrote all of the sections in [Dhalwala et al. \(2022\)](#) and performed all of the simulations. Musaddik Dhalwala wrote all of the sections in [Bayram et al. \(2022\)](#) except the Methodology and performed three of the four simulations found in the paper.

Acknowledgements

This endeavour would not have been possible without the support of many people. Firstly, I would like to thank my supervisor, Dr. Artem Korobenko, for introducing me to the world of finite element methods and computational fluid dynamics. Thank you for assigning me interesting research projects and supporting me during my master's degree. Moreover, thank you for organizing fun summer activities for the lab which greatly helped recharge my mind. I would also like to thank Dr. Peter Oshkai for collaborating with us on the research projects and providing valuable feedback to improve the publications. I am also grateful to the students in the CFSM group for their support during my degree. I would like to thank Ahmed Bayram without who this work would not have been possible. Thank you for helping me understand various aspects of the code and theory, helping me debug many programming problems, and collaborating with me on the research projects. To Haoyang Cen, David Codoni, Sujal Dave, Maryknoll Dsouza, and Eleftherios Tzima, thank you for your help with understanding various topics and making the lab an enjoyable place to work. I would also like to thank my examiners Dr. Marina Gavrilova and Dr. David Wood for their time in reviewing and providing feedback about this work. Lastly, I would like to thank my family for supporting and encouraging me during my degree.

Table of Contents

Abstract	ii
Preface	iii
Acknowledgements	iv
Table of Contents	vi
List of Figures	viii
List of Tables	ix
1 Introduction	1
1.1 Overview of tidal energy	1
1.2 Effect of turbulence on tidal turbines	2
1.2.1 Studies of vertical-axis tidal turbines under a uniform inflow	2
1.2.2 Numerical methods of generating a turbulent inflow	3
1.2.3 Numerical studies of tidal turbines under a turbulent inflow	4
1.3 Effect of a free surface on tidal turbines	5
1.3.1 Methods of modelling a free surface	5
1.3.2 Studies of tidal turbines with free-surface effects	6
1.4 Effect of struts on vertical-axis tidal turbines	7
1.5 Variational multiscale formulation	7
1.6 Organization of thesis	8
2 Methodology	9
2.1 Strong and weak forms of the Navier-Stokes equations for incompressible flows	9
2.2 Level set method	10
2.2.1 Overview of the level set method	10
2.2.2 Level set function	10
2.2.3 Level set equation	11
2.2.4 Smoothed definition of the Heaviside function	11
2.2.5 Signed distance function	11
2.2.6 Reinitialization of the level set function	12
2.2.7 Weak form of the level set equation and reinitialization equation	12
2.3 Residual-based variational multiscale formulation	13
2.4 Weak imposition of Dirichlet boundary condition	16
2.5 Smirnov's random flow generation	17
2.6 Numerical implementation	18

3	Performance and near-wake analysis of a vertical-axis tidal turbine under a turbulent inflow	19
3.1	Validation of Smirnov’s random flow generation method	19
3.1.1	Overview of validation case	19
3.1.2	Computational setup	20
3.1.3	Comparison with experimental and numerical results	22
3.2	Performance evaluation of vertical-axis tidal turbine	23
3.2.1	Computational setup	23
3.2.2	Experimental validation	26
3.2.3	Effect of a turbulent inflow on turbine performance	28
3.3	Near-wake characteristics of the turbine	30
3.3.1	Computational setup	30
3.3.2	Near-wake characteristics under a uniform and turbulent inflow	31
4	Effect of a free surface and different blade-strut configurations on a vertical-axis tidal turbine	38
4.1	Computational setup	38
4.2	Performance comparison of quarter-struts and tip-struts designs under deep immersion	41
4.3	Effect of shallow immersion on free-surface deformation and turbine performance	42
4.4	Differences in the near-wake characteristics	43
5	Conclusions	48
5.1	Effect of turbulence on tidal turbines	48
5.2	Effect of a free surface on tidal turbines	50
5.3	Limitations of the current study	51
	Bibliography	52

List of Figures

3.1	Computational domain of rectangular cylinder in the xy -plane (not to scale).	21
3.2	Slice of the computational mesh in the xy -plane for the rectangular cylinder.	22
3.3	Comparison of pressure coefficient (top) and root mean square of pressure coefficient (bottom) to numerical results of Ricci et al. (2017) and experimental results of Mannini et al. (2017). Lines are colored as follows: current study (-), Ricci et al. (), and Mannini et al. ().	23
3.4	Geometry of 25kW tidal turbine. The dimensions of the geometric parameters are listed in Table 3.2.	24
3.5	Slice of the computational mesh in the xy -plane for the tidal turbine.	26
3.6	Instantaneous power coefficient under a uniform inflow (-) with the mean power coefficient () averaged after the first two revolutions.	27
3.7	Instantaneous power coefficient under a uniform inflow (-) and turbulent inflow with 5% () and 10% () turbulence intensity.	29
3.8	Slice of the computational mesh in the xy -plane for the secondary domain.	31
3.9	Time-averaged velocity deficit and turbulence intensity in the wake of the turbine under a uniform inflow (-) and turbulent inflow with 5% () and 10% () turbulence intensity. Results are obtained in the xy -plane at the midpoint of the turbine blades.	33
3.10	Time-averaged streamwise velocity field (left) and instantaneous vorticity component in the z -direction (right) in the wake of the turbine under different inflow conditions. Slice is taken in the xy -plane at the midpoint of the turbine blades. Note the origin is at the turbine shaft.	35
3.11	Time-averaged turbulent kinetic energy (TKE) in the wake of the turbine under different inflow conditions. Slice is taken in the xz -plane through the center of the turbine. Note the origin is at the turbine shaft.	36
3.12	Instantaneous vorticity isovolumes colored by velocity magnitude in the wake of the turbine under different inflow conditions. Note the origin is at the turbine shaft.	37
4.1	Geometry of 25kW tidal turbine. The dimensions of the geometric parameters are listed in Table 4.1.	39
4.2	Computational domain of turbine in the xy -plane (not to scale).	40
4.3	Slice of the computational mesh in the xz -plane for the tip-struts configuration with a deep-immersion depth of $h = 0.8D$.	41
4.4	Instantaneous power coefficient for quarter-struts configuration under different conditions. Lines are colored as follows: quarter-struts under deep immersion (-), quarter-struts under shallow immersion (), and quarter-struts with no free surface (). Deep and shallow immersion corresponds to $h = 0.8D$ and $h = 0.1D$, respectively.	44
4.5	Instantaneous power coefficient for tip-struts configuration under different conditions. Lines are colored as follows: tip-struts under deep immersion (-) and tip-struts under shallow immersion (). Deep and shallow immersion corresponds to $h = 0.8D$ and $h = 0.1D$, respectively.	45
4.6	Instantaneous streamwise velocity field in the xz -plane for each blade-strut configuration under deep immersion ($h = 0.8D$) and shallow immersion ($h = 0.1D$).	46
4.7	Free surface and instantaneous vorticity isovolumes colored by velocity magnitude for each blade-strut configuration under deep immersion ($h = 0.8D$) and shallow immersion ($h = 0.1D$). Note that for the shallow immersion cases, the free surface has been translated upwards during visualization to keep the same view as the deep immersion cases.	46

4.8 Phase-averaged velocity deficit in the wake of the turbine under deep immersion and shallow immersion for the quarter-struts (-) and tip-struts () configuration. Results are obtained in the xz -plane at the center of the domain. Note the origin is at the turbine shaft. 47

List of Tables

3.1	Comparison of flow characteristics and geometric parameters.	21
3.2	Geometric parameters of 25kW tidal turbine.	24
3.3	Comparison of power coefficient with experimental results.	28
3.4	Comparison of mean power coefficient and standard deviation of power coefficient under a uniform and turbulent inflow.	30
4.1	Geometric parameters of 25kW tidal turbine.	39
4.2	Power coefficient of each blade-strut configuration under different conditions.	45

Chapter 1

Introduction

1.1 Overview of tidal energy

To mitigate the threat of climate change, various goals have been set that promote the advancement of renewable energy technologies. For instance, the Paris Agreement, an ambitious global agreement intended to mitigate global warming, will require significant contribution from the renewable energy sector ([Rogelj et al., 2016](#); [Teske, 2019](#)). According to [Teske \(2019\)](#), the renewable energy sector is expected to contribute approximately 9,500 GW by 2030 and 25,600 GW by 2050 to the total electricity generated. From the various renewable energy sources available, tidal energy has garnered attention due to its high energy density, predictability, and regularity ([Pelc and Fujit, 2002](#); [Widén et al., 2015](#); [Melikoglu, 2018](#)).

Tidal stream technology consists of horizontal-axis (or axial-flow) turbines, vertical-axis (or cross-flow) turbines, and oscillating hydrofoils ([Laws and Epps, 2016](#); [Nachtane et al., 2020](#)). Among these devices, horizontal-axis and vertical-axis turbines are the most mature. Compared to horizontal-axis tidal turbines that have been extensively studied, vertical-axis tidal turbines pose certain advantages that make them an attractive topic for further investigation. For instance, vertical-axis tidal turbines are more suitable in tidal sites with weaker currents ([Laws and Epps, 2016](#); [Melikoglu, 2018](#); [Nachtane et al., 2020](#)). Due to their design, they can also generate energy from any flow direction normal to their axis of rotation ([Laws and Epps, 2016](#)). In the context of turbine arrays, arranging vertical-axis turbines strategically can lead to significantly larger power densities compared to an array of horizontal-axis turbines due to differences in wake characteristics ([Dabiri, 2011](#); [Brownstein et al., 2016](#); [Hezaveh et al., 2018](#); [Brownstein et al., 2019](#)). Although vertical-axis turbines are generally less efficient than horizontal-axis turbines, these advantages merit further investigation of vertical-axis turbines to improve their viability.

1.2 Effect of turbulence on tidal turbines

1.2.1 Studies of vertical-axis tidal turbines under a uniform inflow

This thesis begins by providing a literature review of vertical-axis tidal turbines under a uniform inflow and then discusses studies with a turbulent inflow. Although most numerical studies of tidal turbines are focused on horizontal-axis designs, much work has been done by Marsh et al. to improve the understanding of the complex hydrodynamics of vertical-axis tidal turbines (Marsh et al., 2015b,a, 2017). In Marsh et al. (2017), two- and three-dimensional unsteady Reynolds-averaged Navier-Stokes (URANS) simulations of two vertical-axis tidal turbines are done to determine if two-dimensional simulations are suitable for predicting turbine performance. The results indicated that two-dimensional simulations overpredict the power coefficient as they do not account for the performance reduction due to strut and blade tip effects. Similar findings are reported by Bachant and Wosnik (2014, 2016) who also performed URANS simulations of a vertical-axis turbine. Despite these limitations, two-dimensional URANS simulations may be useful for optimization studies such as investigating the effect of blade pitch angle on the performance of the turbine (Nguyen et al., 2021) and the effect of the number of blades on start-up performance (Sun et al., 2021) due to their low computational cost. A comprehensive study was performed by Gosselin et al. (2016) in which the performance of an H-Darrieus turbine was evaluated as a function of multiple parameters such as Reynolds number, tip speed ratio, solidity, number of blades, blade pitch angle, and blade thickness using two-dimensional URANS simulations. This study also quantified the effects of blade aspect ratio on the efficiency of the turbine using three-dimensional URANS simulations. Some findings of this study include a greater efficiency for turbines with low solidity operating at high Reynolds numbers and a reduction in maximum efficiency for blades with a low aspect ratio. In addition to studies of individual turbines, URANS simulations are also commonly used to study the interaction among turbines in an array (Zanforlin, 2018; Jin et al., 2020; Nag and Sarkar, 2021).

Large eddy simulation (LES) has also been used to study vertical-axis tidal turbines as a more accurate alternative to URANS, although fewer studies are available due to its high computational cost. In Guillaud et al. (2020), LES was used to analyze the effect of solidity on the performance of a vertical-axis turbine. There was no clear benefit in reducing the solidity of the turbine; instead, it was suggested that the optimal solidity is highly dependent on the turbine design. Additionally, simulations were done to investigate the components of the turbine that contribute to its efficiency losses. The blade tips, struts, and blade-strut junctions were found to be the major components responsible for the performance losses of the turbine. Boudreau and Dumas (2017) used Delayed Detached Eddy Simulations (DDES) to compare the wake recovery rates of axial- and cross-flow turbines. The wake of the axial-flow turbine was dominated by the flow instability associated with the tip and root vortices of the blades, which led to enhanced turbulent mixing that promoted wake recovery. Alternatively, the wake dynamics of the cross-flow turbine was strongly affected

by the flow velocity induced by the tip vortices shed during the upstream half of the turbine's rotation cycle, which resulted in a contraction of the central region of the wake in the spanwise direction. Applying the DDES methodology to analysis of the wake dynamics of oscillating-foil turbines, [Boudreau and Dumas \(2018\)](#) revealed similarities to the wake dynamics of cross-flow turbines, where the wake recovery was dominated by the velocity induced by the tip vortices.

1.2.2 Numerical methods of generating a turbulent inflow

One area left for further investigation in numerical studies is the effect of a turbulent inflow on the behaviour of a vertical-axis tidal turbine. In the context of horizontal-axis tidal turbines, experimental studies have been done to investigate the influence of turbulence ([Mycek et al., 2014a,b](#); [Blackmore et al., 2016](#)). There are fewer experimental studies available that investigate the effect of turbulence on the behaviour of a vertical-axis tidal turbine. The effect of turbulence intensity on the performance of a Gorlov Helical turbine was studied in [Bachant and Wosnik \(2011\)](#). Under a turbulent inflow, the mean power coefficient was slightly smaller at higher tip speed ratios and slightly larger at lower tip speed ratios. The performance of full-scale turbines in real sea conditions has also been studied although these studies are scarce. In [Sentchev et al. \(2020\)](#), the power production of a full-scale four-bladed H-Darrieus vertical-axis tidal turbine under real sea conditions is investigated. In agreement with the aforementioned experimental studies ([Mycek et al., 2014a,b](#); [Blackmore et al., 2016](#)), the fluctuations of the power generated increased when the flow became more turbulent. Moreover, the magnitude of the power fluctuations was found to scale linearly with the integral length scale with a large increase in the magnitude when the integral length scale was similar to the turbine size.

The behaviour of a vertical-axis turbine under a turbulent inflow can also be studied numerically, although some thought must be given to prescribe an appropriate inlet velocity field. The two common techniques of prescribing a turbulent inflow are performing a precursor simulation or using a synthetic turbulence generation method. When using the precursor simulation technique, a dataset of inlet boundary conditions for the main simulation are obtained from a section of an auxiliary simulation with the desired flow characteristics. Although the inlet boundary conditions generated from a precursor simulation are highly accurate as they satisfy the Navier-Stokes equations, the precursor technique has certain drawbacks that limit its use. Due to limitations in file storage, a set of inflow data is typically reused which may introduce an artificial low-frequency behaviour into the domain ([Dhamankar et al., 2015](#)). This approach is also inconvenient as a different precursor simulation must be run when a different inlet boundary condition is required. Lastly, it may be prohibitively expensive to perform a precursor simulation for certain applications. Synthetic turbulence generation methods offer a flexible alternative as a turbulent inflow can be generated directly in the main simulation. Moreover, most synthetic turbulence generation methods are capable of generating a turbulent

inflow that matches desired properties such as Reynolds stresses and length scales.

There are several methods of generating synthetic turbulence such as using a Fourier series, proper orthogonal decomposition, digital filtering, and synthetic eddy methods (Tabor and Baba-Ahmadi, 2010). A Fourier series was first used in Kraichnan (1970) to study the diffusion of a particle in an isotropic turbulent velocity field. This method was later modified by Smirnov et al. (2001) and termed the random flow generation (RFG) method. It provides the capability to generate an inhomogeneous, anisotropic turbulent velocity field by applying scaling and coordinate transformations. The resulting velocity field is divergence-free for the case of homogeneous turbulence and nearly divergence-free for the case of inhomogeneous turbulence. Methods using proper orthogonal decomposition have limited applications as they require suitable reference data that is generally taken from experimental measurements or a direct numerical simulation (Tabor and Baba-Ahmadi, 2010; Dhamankar et al., 2015). In digital filtering methods, originally proposed in Klein et al. (2003), a filtering operation is performed on a set of random numbers to obtain a turbulent velocity field with the desired spatial and temporal correlation. This method was modified by Xie and Castro (2008) and Kempf et al. (2012) to improve its computational efficiency, especially for flows with large integral length scales. In contrast to the approaches above, the synthetic eddy method (SEM) (Jarrin et al., 2006, 2009) – an extension of the vortex method (Benhamadouche et al., 2006) – opts for a more physical description of turbulence by populating a virtual box encompassing the inlet with synthetic eddies. These eddies induce a turbulent velocity field at the inlet with specific first- and second-order one-point statistics, spatial and temporal characteristics, and a two-point autocorrelation function (Jarrin et al., 2006). A comprehensive review of synthetic turbulence generation methods can be found in (Tabor and Baba-Ahmadi, 2010; Dhamankar et al., 2015). Apart from proper orthogonal decomposition methods which are limited to simple cases where experimental data is available, the remaining synthetic turbulence generation methods are all used for various applications. They are all sophisticated enough to satisfy the desired properties of the turbulent inflow. Selecting a method comes down to the ability of the method to gracefully adjust to the incompressibility constraint of the Navier-Stokes equations and personal preference.

1.2.3 Numerical studies of tidal turbines under a turbulent inflow

Various numerical methodologies with different synthetic turbulence generation methods have been used to study the effects of turbulence on the behaviour of a tidal turbine, although these studies are limited to horizontal-axis designs (Gant and Stallard, 2008; Afgan et al., 2013; Ahmed et al., 2017; Ahmadi, 2019; Ebdon et al., 2019; Gajardo et al., 2019; Choma et al., 2020; Togneri et al., 2020; Faizan et al., 2022; Grondeau et al., 2022). The wake of such a turbine under a turbulent inflow has been studied using a blade element momentum model (Togneri et al., 2020), Lagrangian Vortex method (Choma et al., 2020), actuator disc model within a URANS framework (Gant and Stallard, 2008), actuator disc model within a detached eddy simulation (DES) framework (Gajardo et al., 2019), and actuator

line model within an LES framework (Ahmadi, 2019). In (Choma et al., 2020), SEM is used to generate a turbulent inflow, while in (Gant and Stallard, 2008; Togneri et al., 2020), both SEM and the von Kármán spectral method (Veers, 1988) are used. The study by Gajardo et al. (2019) uses Smirnov’s RFG to generate a turbulent inflow. Alternatively, instead of using a synthetic turbulence generation method, the study by Ahmadi (2019) uses the mapping technique described by Baba-Ahmadi and Tabor (2009) to prescribe a turbulent inlet. As a higher-fidelity alternative, fully-resolved simulations have been done using RANS, DES, and LES to study the wake and loading of a horizontal-axis turbine under a turbulent inflow generated using SEM (Afgan et al., 2013; Ahmed et al., 2017; Ebdon et al., 2019; Faizan et al., 2022). As can be seen, these studies are all limited to horizontal-axis turbines. To address this gap in the literature, the current work investigates the effect of turbulence on the performance and near-wake characteristics of New Energy Corporation’s 25kW vertical-axis H-Darrieus tidal turbine using the ALE-VMS framework and Smirnov’s RFG method. Using VMS instead of classical LES eliminates any challenges with specifying an appropriate filter for different flows. Moreover, with the residual-based variational multiscale formulation, traditional eddy viscosities that are used to represent turbulent dissipation are not introduced. Although many of the studies discussed above use SEM to generate a turbulent inflow, Smirnov’s RFG is chosen in this work as it can generate a turbulent velocity field that is divergence-free in the case of homogeneous turbulence and nearly divergence-free in the case of inhomogeneous turbulence. This feature provides a great advantage in this study as the governing equations of the flow field are the incompressible Navier-Stokes equations.

1.3 Effect of a free surface on tidal turbines

1.3.1 Methods of modelling a free surface

The second objective of this thesis is to discuss the effect of a free surface on vertical-axis tidal turbines as the depth at which the turbine is installed may affect its performance due to interactions with the free surface. Although studies have been done investigating the effect of a free surface on turbine performance, these studies are mainly limited to horizontal-axis designs. In free-surface flows, the interface separating two fluids is generally a moving and deforming boundary (Katopodes, 2018). As such, in a numerical setting, the location of the interface is determined at every time step. Various methods exist for determining the location of the interface. These methods can be broadly categorized as interface-tracking or interface-capturing methods (Elgeti and Sauerland, 2014).

With interface-tracking methods, the interface is represented explicitly as a set of nodes in the computational mesh (Elgeti and Sauerland, 2014). The location of these nodes is then free to vary depending on the flow velocity. Although interface-tracking methods provide an accurate representation of the interface, certain flow conditions may distort the interface significantly resulting in the need for remeshing (Tezduyar et al., 1998; Elgeti and Sauerland,

2014). Minimizing the frequency of remeshing is highly desirable as it can introduce numerical errors and increase the computational cost of the simulation (Tezduyar et al., 1998; Elgeti and Sauerland, 2014). As a more flexible alternative, interface-capturing methods can be used. With interface-capturing methods, a fixed mesh is used on which the interface is defined implicitly (Elgeti and Sauerland, 2014; Bayram Mohamed et al., 2022). The two fluids and the interface separating them are defined by a scalar field such as the Heaviside function or a signed distance function (Elgeti and Sauerland, 2014). The motion of the free surface is then modelled by an advection equation for this scalar field. Some examples of interface-capturing methods are the marker-and-cell method, volume-of-fluid method, and level set method (Elgeti and Sauerland, 2014).

1.3.2 Studies of tidal turbines with free-surface effects

Most studies that investigate the effect of a free surface on turbine performance involve horizontal-axis tidal turbines. In Whelan et al. (2007), a two-dimensional analytical model was developed to investigate the effect of free-surface proximity on a horizontal-axis turbine. A significant increase in the power coefficient was observed under conditions of high blockage. Similar findings were observed by Consul et al. (2013) where two-dimensional unsteady Reynolds-averaged Navier-Stokes (URANS) simulations were done to investigate the effect of blockage and free-surface deformation on turbine performance. In Bahaj et al. (2007), an experimental study was done to investigate the effect of free-surface proximity on turbine performance. The thrust and power coefficients were found to be lower for the case of shallow immersion compared to deep immersion. Three-dimensional numerical simulations of horizontal-axis turbines under a free surface have also been done. A large eddy simulation (LES) was done by Bai et al. (2014) where the free surface was modelled using the level set method. The results were compared to experimental data with good agreement. In Riglin et al. (2015), a URANS simulation was done where the free surface was modelled using the volume-of-fluid method to investigate the effect of free-surface proximity on turbine performance. The results indicated a large drop in turbine performance near a Froude number of one. Similarly, a URANS simulation with the volume-of-fluid method was done by Hocine et al. (2019) to determine the change in performance between a partially-submerged and fully-submerged Darrieus horizontal-axis turbine. As expected, the turbine was more efficient when it was fully submerged. A comprehensive experimental and numerical study was done by Kolekar and Banerjee (2015) to determine an optimal depth of turbine immersion and investigate the effects of blockage and seafloor proximity on the performance of a horizontal-axis turbine. The experiments were done in a water channel and the numerical study was done using URANS simulations with the volume-of-fluid method. The turbine performance was found to increase as the turbine was moved away from the seafloor up to an optimal depth after which a reduction in performance was observed due to interactions with the free surface. As these studies are focused on studying the effect of a free surface on a horizontal-axis tidal turbine, the present study aims to expand on this body of research by investigating the effect

of free-surface proximity on a vertical-axis tidal turbine.

1.4 Effect of struts on vertical-axis tidal turbines

As horizontal-axis turbines are generally more efficient than vertical-axis turbines, this thesis also studies ways to improve the performance of vertical-axis turbines. There are numerous design parameters that affect their performance. Many studies have been done investigating the effect of solidity, blade design, number of blades, and blade pitch angle on the performance of vertical-axis turbines (Gosselin et al., 2016; Rezaeiha et al., 2018; Guillaud et al., 2020; Nguyen et al., 2021; Sun et al., 2022). The components of a vertical-axis turbine that are detrimental to its performance were also investigated by Guillaud et al. (2020). These components were found to be the blade tips, struts, and blade-strut junctions. To minimize the performance losses due to these components, the effect of strut profile, strut position, and blade-strut junction geometry has been studied (Marsh et al., 2015c; Strom et al., 2018; Villeneuve et al., 2021). In Marsh et al. (2015c), three vertical-axis turbine designs of different strut profiles, blade-strut joints, and strut position were studied using three-dimensional URANS simulations. The strut profile and blade-strut joint design were found to significantly influence the power output while the strut position had a smaller, albeit noticeable impact. The effect of strut position and junction geometry on turbine efficiency was comprehensively studied by performing three-dimensional URANS simulations of various single-blade turbine designs in Villeneuve et al. (2021). In this study, struts located at the tips of the blade (tip-struts) with rounded blade-strut junctions were found to give a higher power coefficient compared to other designs. As this study only considered single-blade turbine designs, future work was suggested to explore performance improvements for multi-bladed turbine designs. Since the performance improvements reported by Villeneuve et al. (2021) are significant, the present study aims to further the work initiated in that study by performing simulations of a full-scale four-bladed vertical-axis tidal turbine with different blade-strut configurations. The effect of a free surface on the performance of each blade-strut configuration is also studied by considering a case of shallow immersion and deep immersion.

1.5 Variational multiscale formulation

From the available LES formulations in the literature, the variational multiscale (VMS) formulation is used in this study. The residual-based variational multiscale (RBVMS) analogue of LES was developed by Bazilevs et al. (2007a). Unlike classical LES which involves filtering of the Navier-Stokes equations, the variational multiscale theory of turbulence modeling is based on a projection of the solution and weighting function space into a coarse- and fine-scale subspace. Resorting to scale separation instead of filtering eliminates any challenges with specifying an appropriate filter for different flows. The fine scales can then be given algebraic descriptions and substituted into the coarse-scale

equations to close the system. With this approach, traditional eddy viscosities that are commonly used to represent turbulent dissipation are not introduced. This formulation was later extended to account for mesh motion using the arbitrary Lagrangian-Eulerian method, hereinafter referred to as ALE-VMS (Bazilevs et al., 2008). Recently, ALE-VMS was used to simulate a vertical-axis tidal turbine under a uniform and turbulent inflow (Bayram et al., 2020; Dhalwala et al., 2022). This study was later extended to test the robustness of the numerical formulation under the effects of cavitation on a tidal turbine in Bayram and Korobenko (2020). A similar study is done using ALE-VMS by Bayram and Korobenko (2021) to study the cavitating flow over a marine propeller. To model a free surface, the ALE-VMS formulation is supplemented with the level set method. The level set method was used successfully within a VMS framework in the context of a horizontal-axis tidal turbine (Yan et al., 2017) and in the context of ship hydrodynamics (Akkerman et al., 2012a,b).

1.6 Organization of thesis

The remainder of this thesis is organized as follows. A description of the computational methodology consisting of the Navier-Stokes equations for incompressible flows, level set method, formulation of the ALE-VMS framework, weak imposition of Dirichlet boundary conditions, and a review of Smirnov's RFG procedure is presented in Chapter 2.

The effects of turbulence on the performance of a vertical-axis tidal turbine is studied first in Chapter 3. In Section 3.1, the implementation of the RFG method within an ALE-VMS framework is validated by comparing to the results of Mannini et al. (2017) and Ricci et al. (2017) for the turbulent flow over a rectangular cylinder with a 5:1 aspect ratio. The performance of the 25kW vertical-axis turbine is studied in Section 3.2 including a validation of the power coefficient with experimental results for a uniform inflow and an investigation of the effects of a turbulent inflow on power production. In Section 3.3, the near-wake characteristics of the turbine under a uniform and turbulent inflow are studied using a multi-domain method.

The effect of a free surface and different blade-strut configurations on a vertical-axis tidal turbine is studied next in Chapter 4. In Sections 4.2 and 4.3, the effect of a free surface on the performance of two blade-strut configurations is studied. A case of deep immersion and shallow immersion is considered for each blade-strut configuration. Moreover, the effect of immersion depth on free-surface deformation and turbine performance is discussed.

Chapter 2

Methodology

2.1 Strong and weak forms of the Navier-Stokes equations for incompressible flows

The governing equations of the flow field are the incompressible Navier-Stokes equations expressed within an arbitrary Lagrangian-Eulerian (ALE) framework as

$$u_{i,i} = 0 \tag{2.1a}$$

$$\rho \left(\partial_t u_i \Big|_{\hat{x}} + (u_j - \hat{u}_j) u_{i,j} - f_i \right) - \sigma_{ij,j} = 0, \tag{2.1b}$$

where Eqs. (2.1a) and (2.1b) are the conservation of mass and momentum, respectively. In these equations, ρ is the density of the fluid, u_i is a component of the flow velocity vector field, \hat{u}_i is a component of the domain velocity vector field, f_i is a component of the body force vector field, and σ_{ij} is a component of the Cauchy stress tensor which is defined as $\sigma_{ij} = -p \delta_{ij} + \mu (u_{i,j} + u_{j,i})$, where p is the pressure, μ is the dynamic viscosity of the fluid, and δ_{ij} is the Kronecker delta. The notation $\Big|_{\hat{x}}$ indicates that the partial time derivative of the flow velocity is taken in a reference domain with coordinates \hat{x} which is a result of the ALE description of the continuum.

The weak form of the governing equations is obtained by first defining an infinite-dimensional trial solution space S for velocity and pressure, and an infinite-dimensional weighting function space V . The weak form can then be stated as follows. Find $\{u_i, p\} \in S$ such that $\forall \{w_i, q\} \in V$, the following bilinear form is satisfied

$$B_{\text{NS}}(\{w_i, q\}, \{u_i, p\}) - F_{\text{NS}}(\{w_i, q\}) = 0, \tag{2.2}$$

where

$$B_{\text{NS}}(\{w_i, q\}, \{u_i, p\}) = \int_{\Omega} w_i \rho \left(\partial_t u_i \Big|_{\hat{x}} + (u_j - \hat{u}_j) u_{i,j} \right) d\Omega + \int_{\Omega} w_{i,j} \sigma_{ij} d\Omega + \int_{\Omega} q u_{j,j} d\Omega \quad (2.3a)$$

$$F_{\text{NS}}(\{w_i, q\}) = \int_{\Omega} w_i \rho f_i d\Omega + \int_{\Gamma} w_i h_i d\Gamma. \quad (2.3b)$$

In Eqs. (2.3a) and (2.3b), $\Omega \subset \mathbb{R}^3$ denotes the three-dimensional spatial domain with a piecewise smooth boundary $\Gamma = \partial\Omega$. The boundary is further decomposed into two non-overlapping subsets Γ^g and Γ^h such that $\Gamma = \Gamma^g \cup \Gamma^h$ where Γ^g and Γ^h denote the subsets on which the velocity and traction h_i are prescribed, respectively. The functions q and w_i are the weighting functions for the conservation of mass and momentum equations, respectively.

2.2 Level set method

2.2.1 Overview of the level set method

To model the free surface, an interface-capturing method, referred to as the level set method, is used. In this method, the interface separating the air and water sections of the domain is represented as the zero level set of a level set function. The motion of the interface is then modelled by a scalar advection equation for the level set function. During this step, the level set function may not retain its original definition. Therefore, the function is reinitialized at every time step to preserve its identity.

2.2.2 Level set function

The level set function ϕ is defined as a continuous scalar function that divides the air and water sections of the domain with a zero level set. The zero level set can be written as

$$\Gamma = \{\mathbf{x} \mid \phi(\mathbf{x}, t) = 0\}. \quad (2.4)$$

The level set function is first given a simple definition where ϕ is arbitrarily defined to be positive in the air section of the domain (Ω_a) and negative in the water section of the domain (Ω_w). Therefore, the level set function becomes

$$\phi(\mathbf{x}, t) = \begin{cases} > 0, & \mathbf{x} \in \Omega_a \\ 0, & \mathbf{x} \in \Gamma \\ < 0, & \mathbf{x} \in \Omega_w \end{cases}, \quad (2.5)$$

where the zero level set Γ represents the free surface. The level set function can then be used along with the Heaviside

function H to write the density and viscosity as,

$$\rho = \rho_w (1 - H(\phi)) + \rho_a H(\phi) \quad (2.6a)$$

$$\mu = \mu_w (1 - H(\phi)) + \mu_a H(\phi). \quad (2.6b)$$

2.2.3 Level set equation

During a numerical simulation with an air-water interface, the interface is generally a moving and deforming boundary. To determine the position of the interface at each time step, the level set equation is solved. The level set equation is an advection equation for the scalar level set function ϕ and can be expressed within an ALE framework as

$$\partial_t \phi \Big|_{\hat{x}} + (u_i - \hat{u}_i) \phi_{,i} = 0. \quad (2.7)$$

With this equation, the level set function is advected by the flow velocity vector field. Therefore, the zero level set – the only level set with a physical significance as it represents the free surface – is deformed according to the flow velocity. That is, the zero level set may consist of different points \mathbf{x} at each time step as the free surface is deformed by the flow velocity.

2.2.4 Smoothed definition of the Heaviside function

Due to the Heaviside function used in Eq. (2.6), there is a discontinuity in fluid properties at the free surface. Such a discontinuity can present problems with stability in numerical solutions. To overcome this problem, the free surface is given a finite width of 2ϵ , where ϵ is of the same order as the element size at the interface. Moreover, the Heaviside function is modified to provide a smooth transition of the fluid properties at the interface as follows (Akkerman et al., 2012b)

$$H(\phi) = \begin{cases} 0, & \phi < -\epsilon \\ \frac{1}{2} \left[1 + \frac{\phi}{\epsilon} + \frac{1}{\pi} \sin\left(\frac{\pi\phi}{\epsilon}\right) \right], & |\phi| \leq \epsilon \\ 1, & \phi > \epsilon \end{cases} \quad (2.8)$$

2.2.5 Signed distance function

To maintain a uniform thickness of the free surface, the requirement, $\|\nabla\phi\| = 1$, must also be imposed. With this requirement, the level set function becomes a signed distance function. Therefore, the level set function initially defined in Eq. 2.5 can be written as

$$\phi(\mathbf{x}, t) = \begin{cases} \min(\|\mathbf{x} - \mathbf{x}_\Gamma\|), & \mathbf{x} \in \Omega_a \\ -\min(\|\mathbf{x} - \mathbf{x}_\Gamma\|), & \mathbf{x} \in \Omega_w \end{cases}, \quad (2.9)$$

where \mathbf{x}_Γ is a point on the zero level set. Note that the level set function is zero by definition for all points that lie on the zero level set.

2.2.6 Reinitialization of the level set function

Recall that the zero level set is advected with the flow velocity according to Eq. (2.7). One drawback of such a procedure is that the condition, $\|\nabla\phi\| = 1$, is not enforced by Eq. (2.7). Therefore, the level set function may not preserve its identity as a signed distance function throughout the simulation. This leads to non-uniformities in the air-water interface thickness, and consequently, irregularities in fluid properties at the interface which causes problems with the stability of the numerical solution (Katopodes, 2018).

To maintain the identity of the level set function as a signed distance function, a reinitialization procedure is applied at every time step. Reinitialization is done by solving the following equation (Akkerman et al., 2012b; Katopodes, 2018)

$$\partial_\tau \phi_d = \text{sgn}(\phi) (1 - \|\nabla\phi_d\|), \quad (2.10)$$

for the reinitialized level set function $\phi_d(\mathbf{x}, t)$. This equation is integrated in pseudo-time τ until steady-state ($\partial_\tau \phi_d = 0$) which ensures $\|\nabla\phi_d\| = 1$ resulting in the level set function returning to a signed distance function.

2.2.7 Weak form of the level set equation and reinitialization equation

Using the same definitions of the infinite-dimensional trial solution space S and the infinite-dimensional weighting function space V from Section 2.1, the weak form of the level set equation and reinitialization equation can be obtained. The weak form of each equation can then be stated as follows. Find $\{\phi, \phi_d\} \in S$ such that $\forall \{\eta, \eta_d\} \in V$, the following bilinear form is satisfied

$$B_{\text{LS}}(\eta, \phi) = 0 \quad (2.11a)$$

$$B_{\text{RI}}(\eta_d, \phi_d) - F_{\text{RI}}(\eta_d, \phi_d) = 0, \quad (2.11b)$$

where

$$B_{\text{LS}}(\eta, \phi) = \int_{\Omega} \eta \left(\partial_i \phi \Big|_{\hat{x}} + (u_i - \hat{u}_i) \phi_{,i} \right) d\Omega \quad (2.12a)$$

$$B_{\text{RI}}(\eta, \phi_d) = \int_{\Omega} \eta_d \left(\partial_{\tau} \phi_d + \text{sgn}(\phi) \sqrt{\phi_{d,i} \phi_{d,i}} \right) d\Omega \quad (2.12b)$$

$$F_{\text{RI}}(\eta, \phi_d) = \int_{\Omega} \eta_d \text{sgn}(\phi) d\Omega. \quad (2.12c)$$

In these equations, the functions η and η_d are the weighting functions for the level set and reinitialization equations, respectively.

2.3 Residual-based variational multiscale formulation

To permit a numerical implementation of Eq. (2.2), the infinite-dimensional spaces S and V are decomposed into a resolved coarse-scale sub-space denoted by an h -superscript and an unresolved subgrid-scale sub-space denoted by a prime-superscript ($'$) such that $S = S^h \oplus S'$ and $V = V^h \oplus V'$. Such a scale separation indicates that the coarse scales are those represented in the calculation; that is, they consist of all Fourier modes below some cut-off wave number. Meanwhile, the subgrid scales consist of all remaining Fourier modes and therefore require an approximation. The solution variables and weighting functions are also decomposed into the two sub-spaces: $u_i = u_i^h + u_i'$, $p = p^h + p'$, $\phi = \phi^h + \phi'$, $\phi_d = \phi_d^h + \phi_d'$, $w_i = w_i^h + w_i'$, $q = q^h + q'$, $\eta = \eta^h + \eta'$, and $\eta_d = \eta_d^h + \eta_d'$. Although such a scale separation results in a finite-dimensional system for the coarse-scale component of the solution, the subgrid-scale component of the solution is still an infinite-dimensional system (Bazilevs et al., 2007b). To overcome this problem, an approximation of the subgrid-scale component of the solution must be obtained.

Early works using the variational multiscale formulation modelled the subgrid-scale component of the solution using eddy viscosities as is done in classical LES (Gravemeier, 2006; Bazilevs et al., 2007b). While such an approach has been used successfully (Gravemeier, 2006), the residual-based variational multiscale (RBVMS) formulation is used in the present study as it avoids the use of ad hoc eddy viscosities (Bazilevs et al., 2007b). In RBVMS, the turbulence modelling consists of approximating the subgrid-scale component of the solution with an analytical representation. An algebraic description of the subgrid-scale solution variables in terms of the residuals of the coarse-scale equations is provided in (Bazilevs et al., 2007b) as

$$\begin{pmatrix} u'_i \\ p' \\ \phi' \\ \phi'_d \end{pmatrix} = - \begin{pmatrix} \tau_M (r_M)_i \\ \tau_C r_C \\ \tau_\phi r_\phi \\ \tau_{\phi_d} r_{\phi_d} \end{pmatrix}, \quad (2.13)$$

where $(r_M)_i$, r_C , r_ϕ , and r_{ϕ_d} are the residuals of the coarse-scale momentum, continuity, level set, and reinitialization equations, respectively, defined as

$$(r_M)_i = \rho \left(\partial_t u_i^h \Big|_{\hat{x}} + (u_j^h - \hat{u}_j^h) u_{i,j}^h - f_i^h \right) - \sigma_{i,j}^h, \quad (2.14a)$$

$$r_C = u_{i,i}^h, \quad (2.14b)$$

$$r_\phi = \partial_t \phi^h \Big|_{\hat{x}} + (u_i^h - \hat{u}_i^h) \phi_{,i}^h, \quad (2.14c)$$

$$r_{\phi_d} = \partial_\tau \phi_d^h - \left(2H(\phi^h) - 1 \right) \left(1 - \sqrt{\phi_{d,i}^h \phi_{d,i}^h} \right). \quad (2.14d)$$

In Eq. (2.13), τ_M , τ_C , τ_ϕ , and τ_{ϕ_d} are conventional stabilization parameters discussed in (Brooks and Hughes, 1982; Akin et al., 2003; Tezduyar and Sathe, 2003; Bazilevs et al., 2007b; Tezduyar et al., 2008a; Hsu et al., 2010; Akkerman et al., 2012b; Takizawa et al., 2018). Note that in Eq. (2.14d), $\text{sgn}(\phi^h)$ is replaced with $2H(\phi^h) - 1$ to account for the modified definition of the Heaviside function in Section 2.2.4. The decomposition of the solution variables and weighting functions are substituted into Eqs. (2.2) and (2.11) along with the subgrid-scale solution variables defined in Eq. (2.13). After discretizing the resulting equation in space using n_{el} linear finite elements where $\Omega = \bigcup_{e=1}^{n_{\text{el}}} \Omega^e$, the semi-discrete ALE-VMS formulation can be stated as follows. Find $\{u_i^h, p^h, \phi^h, \phi_d^h\} \in S^h$ such that $\forall \{w_i^h, q^h, \eta^h, \eta_d^h\} \in V^h$, the following bilinear forms are satisfied

$$B_{\text{NS}}(\{w_i^h, q^h\}, \{u_i^h, p^h\}) - F_{\text{NS}}(\{w_i^h, q^h\}) = 0 \quad (2.15a)$$

$$B_{\text{LS}}(\eta, \phi) = 0 \quad (2.15b)$$

$$B_{\text{RI}}(\eta_d, \phi_d) - F_{\text{RI}}(\eta_d, \phi_d) = 0, \quad (2.15c)$$

where the terms for the Navier-Stokes equations are defined as

$$\begin{aligned} B_{\text{NS}}(\{w_i^h, q^h\}, \{u_i^h, p^h\}) &= \int_{\Omega} w_i^h \rho \left(\partial_t u_i^h \Big|_{\hat{x}} + (u_j^h - \hat{u}_j^h) u_{i,j}^h \right) d\Omega \\ &+ \int_{\Omega} w_{i,j}^h \sigma_{ij}^h d\Omega + \int_{\Omega} q^h u_{j,j}^h d\Omega \end{aligned}$$

$$\begin{aligned}
& + \sum_{e=1}^{n_{el}} \int_{\Omega^e} \tau_M \left((u_j^h - \hat{u}_j^h) w_{i,j}^h + \frac{1}{\rho} q_i^h \right) (r_M)_i \, d\Omega \\
& + \sum_{e=1}^{n_{el}} \int_{\Omega^e} \rho \tau_C w_{i,i}^h r_C \, d\Omega - \sum_{e=1}^{n_{el}} \int_{\Omega^e} \tau_M w_i^h (r_M)_j u_{i,j}^h \, d\Omega \\
& - \sum_{e=1}^{n_{el}} \int_{\Omega^e} \frac{1}{\rho} w_{i,j}^h \tau_M (r_M)_i \tau_M (r_M)_j \, d\Omega
\end{aligned} \tag{2.16a}$$

$$F_{NS}(\{w_i^h, q^h\}) = \int_{\Omega} w_i^h \rho f_i^h \, d\Omega + \int_{\Gamma^h} w_i^h h_i \, d\Gamma, \tag{2.16b}$$

the term for the level set equation is defined as

$$\begin{aligned}
B_{LS}(\eta^h, \phi^h) &= \int_{\Omega} \eta^h \left(\partial_t \phi^h|_{\mathbf{x}} + (u_i^h - \hat{u}_i^h) \phi_{,i}^h \right) \, d\Omega \\
& + \sum_{e=1}^{n_{el}} \int_{\Omega^e} \tau_{\phi} (u_i^h - \hat{u}_i^h) \eta_{,i}^h r_{\phi} \, d\Omega + \sum_{e=1}^{n_{el}} \int_{\Omega^e} \eta_{,i}^h k_{dc} \phi_{,i}^h \, d\Omega,
\end{aligned} \tag{2.17}$$

and the terms for the reinitialization equation are defined as

$$\begin{aligned}
B_{RI}(\eta_d^h, \phi_d^h) &= \int_{\Omega} \eta_d^h \left(\partial_{\tau} \phi_d^h + c_i^h \phi_{d,i}^h \right) \, d\Omega \\
& + \sum_{e=1}^{n_{el}} \int_{\Omega^e} \tau_{\phi_d} c_i^h \eta_{d,i}^h \left(\partial_{\tau} \phi_d^h + c_i^h \phi_{d,i}^h \right) \, d\Omega \\
& + \sum_{e=1}^{n_{el}} \int_{\Omega^e} \eta_{d,i}^h \tilde{k}_{dc} \phi_{d,i}^h \, d\Omega
\end{aligned} \tag{2.18a}$$

$$F_{RI}(\eta_d^h) = \int_{\Omega} \eta_d^h \left(2H(\phi^h) - 1 \right) \, d\Omega + \sum_{e=1}^{n_{el}} \int_{\Omega^e} \tau_{\phi_d} \left(2H(\phi^h) - 1 \right) c_i^h \eta_{d,i}^h \, d\Omega, \tag{2.18b}$$

where c_i is a component of the advection velocity vector field of the reinitialization equation defined as

$$c_i = \left(2H(\phi^h) - 1 \right) \frac{\phi_{d,i}^h}{\sqrt{\phi_{d,j}^h \phi_{d,j}^h}}. \tag{2.19}$$

The stabilization parameters in Eqs. (2.16) – (2.18) are defined as

$$\tau_M = \left(\frac{4}{\Delta t^2} + (u_i^h - \hat{u}_i^h) G_{ij} (u_j^h - \hat{u}_j^h) + C_I \left(\frac{\mu}{\rho} \right)^2 G_{ij} G_{ij} \right)^{-1/2} \tag{2.20a}$$

$$\tau_C = (G_{ii} \tau_{\mathbf{u}})^{-1} \tag{2.20b}$$

$$\tau_{\phi} = \left(\frac{4}{\Delta t^2} + (u_i^h - \hat{u}_i^h) G_{ij} (u_j^h - \hat{u}_j^h) \right)^{-1/2} \tag{2.20c}$$

$$\tau_{\phi_d} = \left(\frac{4}{\Delta \tau^2} + c_i^h G_{ij} c_j^h \right)^{-1/2}, \tag{2.20d}$$

where Δt is the time step, $\Delta \tau$ is the pseudo-time step of the reinitialization equation, G_{ij} is a component of the element metric tensor, and C_I is a positive constant equal to three derived from an element-wise inverse estimate (Bazilevs et al., 2007b). To improve the stability of the level set and reinitialization equations, residual-based discontinuity capturing operators (Tezduyar, 2003, 2007; Tezduyar and Senga, 2007; Tezduyar et al., 2008b; Codoni et al., 2021, 2022) are used. They are defined as

$$k_{dc} = C_\phi \frac{|r_\phi|}{\sqrt{\phi_{,i}^h G_{ij} \phi_{,j}^h}} \quad (2.21a)$$

$$\tilde{k}_{dc} = C_{\phi_d} \frac{|r_{\phi_d}|}{\sqrt{\phi_{d,i}^h G_{ij} \phi_{d,j}^h}}, \quad (2.21b)$$

where C_ϕ and C_{ϕ_d} are positive constants of the order $\mathcal{O}(-1)$.

2.4 Weak imposition of Dirichlet boundary condition

The ALE-VMS formulation is augmented with a weak imposition of the Dirichlet boundary condition $u_i = g_i$, where g_i is a component of the prescribed velocity vector field at boundaries where a Dirichlet boundary condition is imposed (Bazilevs and Hughes, 2007; Bazilevs et al., 2007c). This approach serves an analogous purpose to using wall functions in RANS or conventional LES frameworks; i.e., for cases in which a highly resolved boundary layer refinement is not feasible, the Dirichlet boundary condition can be weakly imposed to relax the mesh resolution requirements at no-slip surfaces. To weakly impose the Dirichlet boundary condition, the following terms are added to the left-hand side of Eq. (2.15)

$$\begin{aligned} & - \sum_{b=1}^{n_{\text{eb}}} \int_{\Gamma^b \cap \Gamma^g} w_i^h \sigma_{ij}^h n_j \, d\Gamma - \sum_{b=1}^{n_{\text{eb}}} \int_{\Gamma^b \cap \Gamma^g} (\mu (w_{i,j}^h + w_{j,i}^h) n_j + q^h n_i) (u_i^h - g_i^h) \, d\Gamma \\ & - \sum_{b=1}^{n_{\text{eb}}} \int_{\Gamma^b \cap (\Gamma^g)^-} w_i^h \rho u_j^h n_j (u_i^h - g_i^h) \, d\Gamma \\ & + \sum_{b=1}^{n_{\text{eb}}} \int_{\Gamma^b \cap \Gamma^g} \tau_B w_i^h (u_i^h - g_i^h) \, d\Gamma, \end{aligned} \quad (2.22)$$

where n_{eb} denotes the number of boundary elements, n_i is a component of the outward unit normal vector, and τ_B is a stabilization parameter discussed in (Bazilevs et al., 2007c). Note the boundary Γ^g has been decomposed into n_{eb} boundary elements where each element is denoted by Γ^b and the part of Γ^g corresponding to an inflow is defined as $(\Gamma^g)^- = \{\mathbf{x} \mid (u_i^h - \hat{u}_i^h) n_i < 0, \forall \mathbf{x} \in \Gamma^g\}$.

2.5 Smirnov's random flow generation

As with classical LES, some technique must be applied to prescribe a turbulent inflow in the ALE-VMS framework. In this study, a synthetic turbulence generation method referred to as Smirnov's random flow generation (RFG) is used. From the numerous synthetic turbulence generation methods available, Smirnov's RFG was chosen as it can generate a turbulent velocity field that is divergence-free for the case of homogeneous turbulence and nearly divergence-free for the case of inhomogeneous turbulence. A divergence-free velocity field ensures compatibility with the incompressible Navier-Stokes equations that govern the flow field. A brief review of Smirnov's RFG method (Smirnov et al., 2001) is provided below. The method consists of generating a continuous intermediate velocity field, whose components are denoted by v_i , using a superposition of harmonic functions. A scaling operation and orthogonal transformation is then applied to this intermediate velocity field to obtain a velocity field that satisfies the specified velocity correlation tensor. The result is a time-dependent velocity field, whose components are denoted by u_i , with a specified velocity correlation tensor with components r_{ij} , integral length scale of turbulence ℓ which can be thought of as the size of the eddy, and integral time scale of turbulence τ . In the equations below, parentheses around indices preclude summation.

First, an orthogonal tensor with components a_{ij} that would diagonalize a specified velocity correlation tensor expressed in component form as $r_{ij} = \overline{u'_i u'_j}$, where u'_i is the fluctuating component of the flow velocity vector field, is found

$$a_{mi} a_{nj} r_{ij} = c_{(n)}^2 \delta_{mn}, \quad (2.23)$$

where the coefficients $\{c_n\}_{n=1}^3$ constitute a vector with components equal to the square root of the eigenvalues of the velocity correlation tensor, respectively.

An intermediate velocity field at a position \mathbf{x} and time t is then generated using a superposition of harmonic functions

$$v_i(\mathbf{x}, t) = \sqrt{\frac{2}{N}} \sum_{n=1}^N \left[p_i^n \cos(\tilde{k}_j^n \tilde{x}_j + \omega_n \tilde{t}) + q_i^n \sin(\tilde{k}_j^n \tilde{x}_j + \omega_n \tilde{t}) \right], \quad (2.24)$$

$$\tilde{x}_j = \frac{x_j}{\ell}, \quad \tilde{t} = \frac{t}{\tau}, \quad \tilde{k}_j^n = k_j^n \frac{\ell/\tau}{c_{(j)}}, \quad (2.25)$$

$$p_i^n = \epsilon_{ijm} \zeta_j^n k_m^n, \quad q_i^n = \epsilon_{ijm} \xi_j^n k_m^n, \quad (2.26)$$

$$\zeta_i^n, \xi_i^n, \omega_n \in N(0, 1), \quad k_i^n \in N(0, 1/2), \quad (2.27)$$

where N is the spectral sample size, ϵ_{ijk} is the Levi-Civita symbol and $N(M, S)$ is a normal distribution with mean M and standard deviation S . The parameters ζ_i^n and ξ_i^n represent random numbers taken from a normal distribution with a mean of zero and standard deviation of one. The modeled turbulence spectrum below is characterized by the components k_i^n of the wave-number vectors and values ω_n of the frequency,

$$E(k) = 16(2/\pi)^{1/2} k^4 \exp(-2k^2). \quad (2.28)$$

A scaling operation is applied in Eq. (2.29) to obtain another intermediate velocity field whose components are denoted by w_i before the final velocity field is obtained in Eq. (2.30) from an orthogonal transformation

$$w_i = c_{(i)} v_{(i)}, \quad (2.29)$$

$$u_i = a_{ij} w_j. \quad (2.30)$$

Smirnov et al. showed that the generated velocity field is divergence-free in the case of homogeneous turbulence and nearly divergence-free in the case of inhomogenous turbulence (Smirnov et al., 2001). To maintain consistency with Smirnov et al. (2001), a spectral sample size of $N = 1000$ is used in this study.

2.6 Numerical implementation

Equation (2.15) forms a semi-discrete non-linear time-dependent system of partial differential equations that is advanced in time using the second-order generalized- α method (Chung and Hulbert, 1993; Jansen et al., 2000). The discrete non-linear system of equations at each time step is linearized using the Newton-Raphson method and the resulting linear system is solved iteratively using the sparse generalized minimum residual (GMRES) algorithm (Saad, 2003). The stopping criteria of the GMRES algorithm is based on a specified tolerance of the L_2 -norm of the linear system while the stopping criteria of the Newton-Raphson iterations is based on a specified tolerance of the L_2 -norm of the residuals of the mass and momentum conservation equations.

Chapter 3

Performance and near-wake analysis of a vertical-axis tidal turbine under a turbulent inflow

In this chapter, the effects of a turbulent inflow on the performance of a vertical-axis tidal turbine is studied. In Section 3.1, the implementation of Smirnov's random flow generation (RFG) method within an arbitrary Lagrangian-Eulerian variational multiscale (ALE-VMS) framework is validated by comparing to the results of [Mannini et al. \(2017\)](#) and [Ricci et al. \(2017\)](#) for the turbulent flow over a rectangular cylinder with a 5:1 aspect ratio. The performance of a 25kW vertical-axis tidal turbine is studied in Section 3.2 including a validation of the power coefficient with experimental results for a uniform inflow and an investigation of the effects of a turbulent inflow on power production. In Section 3.3, the near-wake characteristics of the turbine under a uniform and turbulent inflow are studied using a multi-domain method.

3.1 Validation of Smirnov's random flow generation method

3.1.1 Overview of validation case

The implementation of Smirnov's RFG method in the ALE-VMS framework is first validated by simulating a turbulent flow over a rectangular cylinder with a 5:1 aspect ratio. This validation case is referred to as a benchmark on the aerodynamics of a rectangular 5:1 cylinder (BARC). Although the geometry of a rectangular cylinder is incredibly simple, the resulting flow field is complex as it consists of unsteady flow separation at the leading edge and reattach-

ment downstream (Bruno et al., 2014). A review of the contributions to this benchmark study is provided in Bruno et al. (2014). Recently, Mannini et al. (2017) investigated the effects of freestream turbulence on the aerodynamic behaviour of the rectangular cylinder in a wind tunnel. Ricci et al. (2017) also studied this benchmark case under a turbulent inflow using LES with a similar synthetic turbulence generation method. The present results are compared to those from (Mannini et al., 2017; Ricci et al., 2017) to validate the implementation of Smirnov’s RFG method.

3.1.2 Computational setup

As in Ricci et al. (2017), the flow is characterized by a depth-based Reynolds number of $Re_D = U_\infty D / \nu = 5.5 \times 10^4$, where U_∞ is the freestream velocity and D is the depth of the cylinder. The reader is referred to Fig. 3.1 and Table 3.1 for the dimensions of the cylinder. Additionally, the turbulent velocity field is assumed to be homogeneous and isotropic with a turbulence intensity and turbulence length scale of $T_i = 2.9\%$ and $L = 1.3D$, respectively (Mannini et al., 2017; Ricci et al., 2017). Following the procedure of Yan and Li (2015) and Buffa et al. (2021), a simulation is first performed in an empty domain to evaluate the streamwise decay of turbulence intensity. The turbulence intensity prescribed at the inlet is then scaled such that the desired turbulence intensity of 2.9% is obtained at the axis of the cylinder.

The computational domain matches that of Ricci et al. (2017) and a slice in the xy -plane is shown in Fig. 3.1. The aspect ratio of the rectangular cylinder is $B/D = 5$ and the distance from the inlet to the front face of the cylinder is $\Lambda = 16B$. The dimensions of the domain are a length of $D_x = 40B$, height of $D_y = 30B$, and width of $D_z = B$. The flow characteristics and geometric parameters in the current study are compared to the numerical study of Ricci et al. (2017) and the experimental study of Mannini et al. (2017) in Table 3.1 for convenience.

As a summary, the variables in Table 3.1 are described here. The variables D_x , D_y , and D_z refer to the size of the computational domain along each axis. The aspect ratio (chord-to-depth ratio) of the cylinder is B/D . The distance from the inlet to the front face of the cylinder is Λ . The depth-based Reynolds number, turbulence intensity, and turbulence length scale are denoted by Re_D , T_i , and L , respectively. In Table 3.1, the top two rows are identical as the size of the computational domain for the current simulation was chosen to match the size of the computational domain for the LES simulation of Ricci et al. (2017) to allow for a fair comparison. The third row is included only for convenience to provide details about the experimental setup.

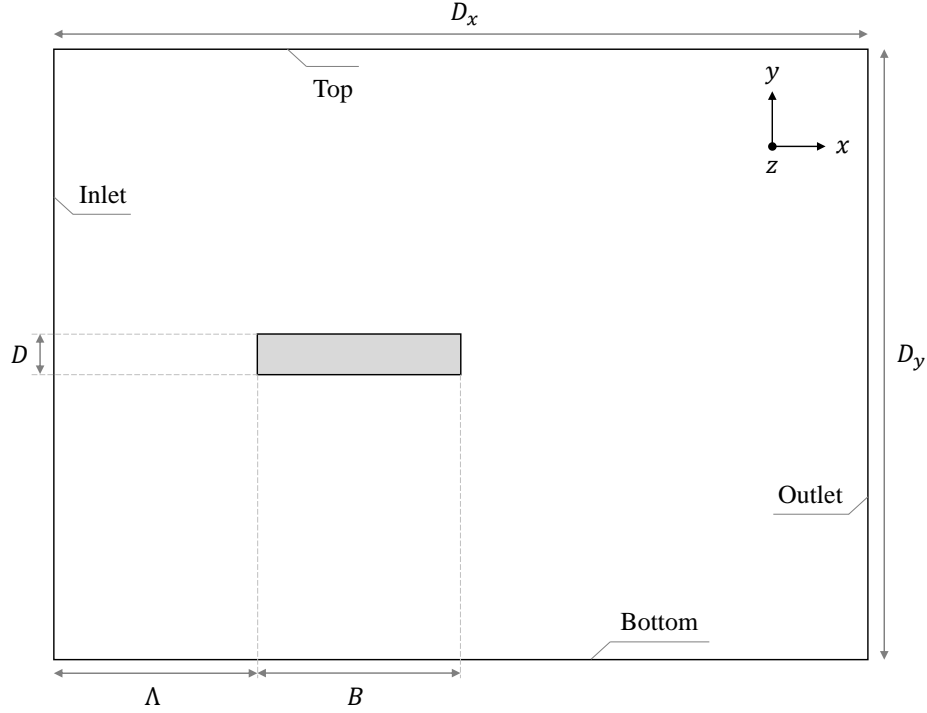


Figure 3.1: Computational domain of rectangular cylinder in the xy -plane (not to scale).

Table 3.1: Comparison of flow characteristics and geometric parameters.

Source	D_x/B	D_y/B	D_z/B	B/D	Λ/B	Re_D	T_i (%)	L/D
Current study	40	30	1	5	16	5.50×10^4	2.9	1.3
Ricci et al. (2017)	40	30	1	5	16	5.50×10^4	2.9	1.3
Mannini et al. (2017)	73	5	8	5	-	$5.59 \times 10^4 - 6.00 \times 10^4$	2.9	1.3

A turbulent velocity field is prescribed at the inlet boundary according to Smirnov's RFG method, while a traction-free boundary condition is prescribed at the outlet boundary. At the top, bottom, and side boundaries, a no-penetration boundary condition is imposed. The no-slip boundary condition is imposed weakly on the cylinder surface according to the formulation of Section 2.4 to relax the mesh resolution requirements of the boundary layer.

The volumetric mesh consists of prism and hexahedral elements. To reduce the numerical dissipation of the turbulent velocity field prescribed at the inlet, a finer mesh refinement is used at the central section of the domain as shown in Fig. 3.2. The non-dimensional time step is $\Delta t^* = (U_\infty / D) \Delta t = 5 \times 10^{-3}$ resulting in a maximum CFL number less than 5.

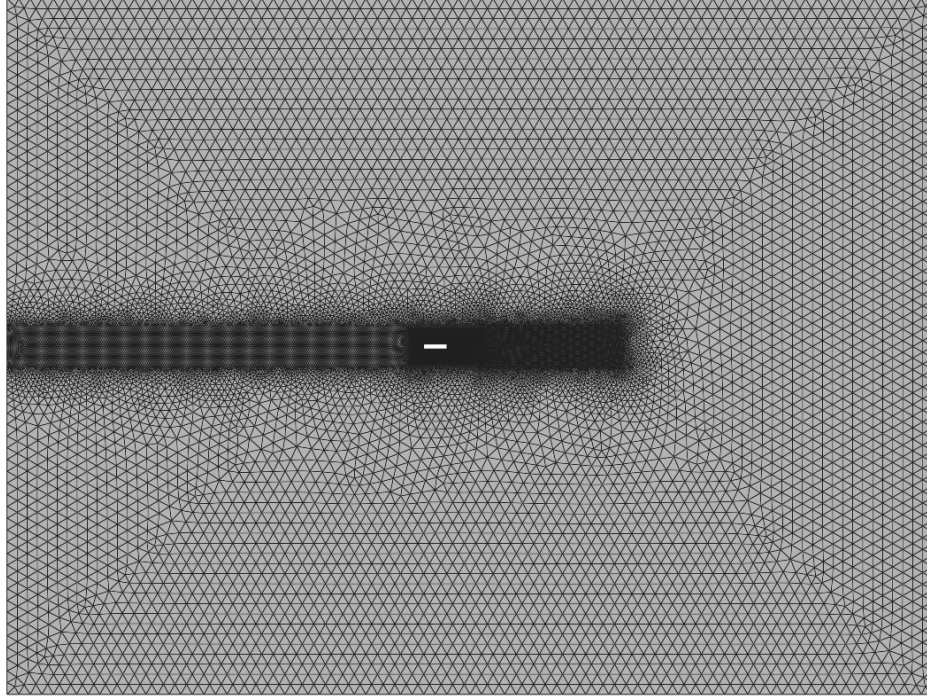


Figure 3.2: Slice of the computational mesh in the xy -plane for the rectangular cylinder.

3.1.3 Comparison with experimental and numerical results

A comparison of the pressure coefficient (C_p) and root mean square (rms) of the pressure coefficient (C'_p) over the top-half of the central section of the rectangular cylinder with the results of Ricci et al. (2017) and Mannini et al. (2017) is provided in Fig. 3.3. The pressure coefficient agrees fairly well for each study while some discrepancy exists for the rms of the pressure coefficient. The rms of the pressure coefficient found by Ricci et al. (2017) is slightly over-predicted near the center. In contrast, the rms of the pressure coefficient of the current study is slightly under-predicted in certain regions. The discrepancies between the current study and that of Ricci et al. (2017) may be attributed to differences in the numerical formulation and synthetic turbulence generation method. Despite these differences, both results are in fairly good agreement with the experimental results of Mannini et al. (2017). Therefore, the RFG method is used to study the effect of a turbulent inflow on the performance of the vertical-axis turbine.

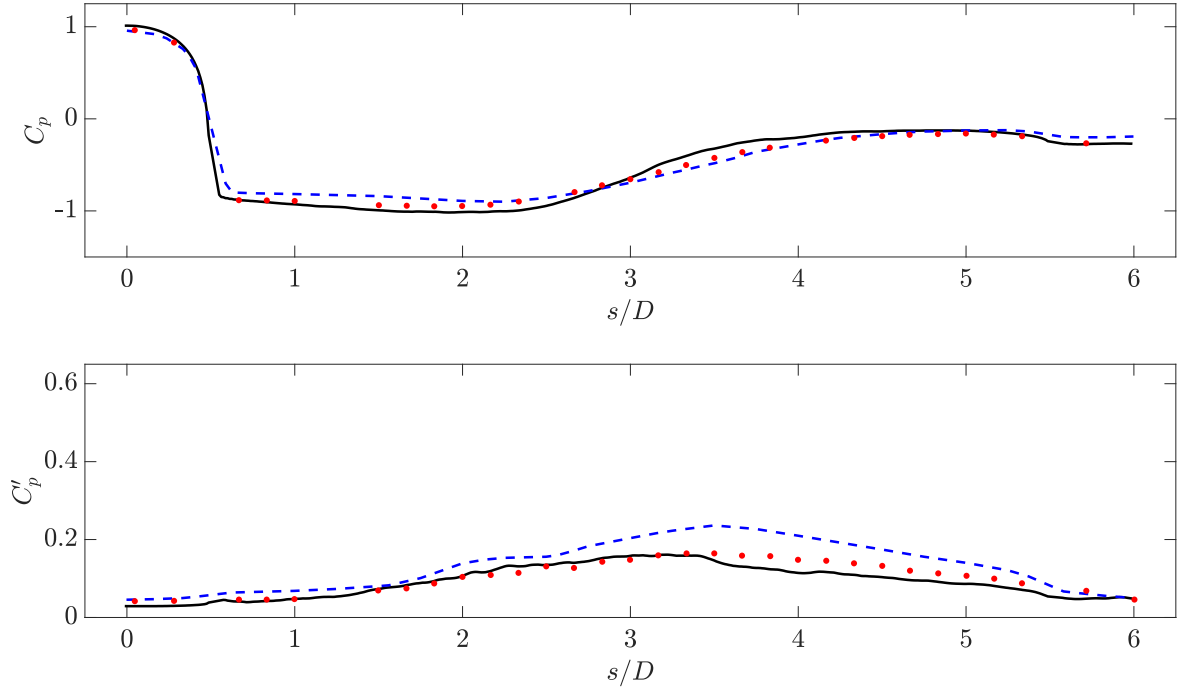


Figure 3.3: Comparison of pressure coefficient (top) and root mean square of pressure coefficient (bottom) to numerical results of Ricci et al. (2017) and experimental results of Mannini et al. (2017). Lines are colored as follows: current study (—), Ricci et al. (---), and Mannini et al. (···).

3.2 Performance evaluation of vertical-axis tidal turbine

3.2.1 Computational setup

The turbine is designed and manufactured by [New Energy Corporation](#) and is shown in Fig. 3.4. It is a 25kW four-bladed H-Darrieus vertical-axis tidal turbine with a rotor diameter (D) of 3.4m, blade span (b) of 1.7m, and shaft height (s) of 3.9m. A NACA 0021 profile with a chord length (c) of 0.254m is used for the blades and struts, and the blades are pitched at a 4° angle of attack. The geometric parameters of the turbine are summarized in Table 3.2 for convenience. The operating condition studied is provided by [New Energy Corporation](#). The mean inflow velocity (u_∞) is 3.0m/s and the rotational speed of the turbine (Ω) is 35rpm. The tip speed ratio of the turbine, defined as $\lambda = (0.5 \Omega D)/u_\infty$ is 2.08.

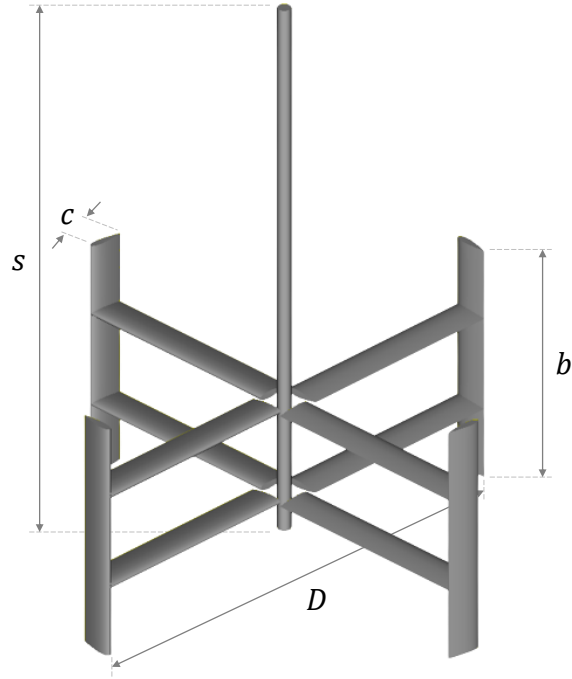


Figure 3.4: Geometry of 25kW tidal turbine. The dimensions of the geometric parameters are listed in Table 3.2.

Table 3.2: Geometric parameters of 25kW tidal turbine.

Parameter	Value
Blade/Strut Profile	NACA 0021
Rotor Diameter (D)	3.4m
Blade Span (b)	1.7m
Shaft Height (s)	3.9m
Chord Length (c)	0.254m
Aspect Ratio (b/c)	6.7
Blade Pitch Angle	4°

A slice of the mesh in the xy -plane is shown in Fig. 3.5. In the previous studies where ALE-VMS was used to study the performance of a 5kW vertical-axis tidal turbine under uniform inflow conditions (Bayram et al., 2020; Bayram and Korobenko, 2020), the sliding interface technique described in Bazilevs and Hughes (2008) is used. Although the sliding interface technique has shown its accuracy and robustness in various applications, the use of this technique significantly increases the computational cost of the simulation. Therefore, in this study, an ALE description of the

continuum is used which allows domain motion while capturing the flow field independently of this domain motion. The left-hand side of the boundary of the cylindrical domain is treated as the inlet while the right-hand side is treated as the outlet. A uniform velocity field or turbulent velocity field according to Smirnov's RFG method is prescribed at the inlet while a traction-free boundary condition is prescribed at the outlet. A no-penetration boundary condition is prescribed at the top and bottom boundaries of the cylindrical domain. The no-slip boundary condition is imposed weakly on the blades, struts, and shaft such that the flow velocity and mesh velocity are equal on these surfaces.

To select appropriate parameters for the turbulent velocity field, literature characterizing the turbulence at various tidal energy sites is investigated. [Milne et al. \(2016\)](#) summarized the turbulence properties at various tidal sites. Although turbulence properties are expected to be site-specific, such a summary is useful for obtaining typical values. In the tidal sites considered in [Milne et al. \(2016\)](#), the median streamwise turbulence intensities were between 5-18%. [Milne et al. \(2013\)](#) also conducted a study of the turbulence characteristics at the Sound of Islay. They reported the ratios of the standard deviations of the lateral (σ_v) and vertical (σ_w) velocity fluctuations to the streamwise (σ_u) velocity fluctuations which provide a measure of the turbulence anisotropy at the tidal site. These ratios were found to be $\sigma_u : \sigma_v : \sigma_w = 1 : 0.75 : 0.56$. [Milne et al. \(2013\)](#) also compared these ratios to those presented by [Nezu and Nakagawa \(1993\)](#) of $1 : 0.71 : 0.55$ for two-dimensional open-channel flows at a Reynolds number of $Re \approx 10^4$. It is interesting to note that the two sets of ratios are in great agreement with each other despite differences in bathymetry and Reynolds numbers ([Milne et al., 2013](#)). In this paper, low and moderate turbulence intensities of 5% and 10% are considered with the anisotropic ratio observed by [Milne et al. \(2013\)](#) of $\sigma_u : \sigma_v : \sigma_w = 1 : 0.75 : 0.56$. Note the turbulence intensity is defined as $T_i = (2k/3)^{1/2} / u_\infty$, where k is the turbulent kinetic energy and u_∞ is the freestream velocity.

Along with the turbulence intensity and anisotropic ratios, the integral length and time scales of turbulence are also important in characterizing the spatial and temporal structure of turbulence, respectively. [Milne et al. \(2013\)](#) and [McCaffrey et al. \(2015\)](#) evaluated the velocity autocorrelation function to obtain the integral time scales of turbulence and then invoked Taylor's frozen turbulence hypothesis ([Taylor, 1938](#)) to estimate the integral length scales of turbulence at a tidal site. [McCaffrey et al. \(2015\)](#) found the mean streamwise integral length scale to be 11.6m and the maximum streamwise integral length scale to be 81m suggesting the presence of a broad range of length scales in tidal sites. [Milne et al. \(2013\)](#) found the mean streamwise integral length scales to be 11.3m and 14.6m during flood and ebb tide, respectively. The ratios of the transverse and vertical integral time scales to the streamwise integral time scale were approximately 0.2. As reports of integral scales at tidal sites are scarce in the literature, these studies are helpful in selecting approximate values that correspond to a typical tidal site. Based on these studies, the streamwise integral length scale (L_u) was chosen to be 10m, and the transverse and vertical integral length scales were chosen to be $0.2L_u$ as was observed by [Milne et al. \(2013\)](#). Moreover, the integral time scales were approximated by invoking Taylor's frozen turbulence hypothesis ([Taylor, 1938](#)) as done in ([Milne et al., 2013](#); [McCaffrey et al., 2015](#)). As research into

the turbulence characteristics at tidal sites continues, site-specific scales can be considered in the future to improve the accuracy of simulations.

The mesh shown in Fig. 3.5 was built according to the study in Bayram et al. (2020) for a 5kW vertical-axis tidal turbine under similar operating conditions. In Bayram et al. (2020), a grid convergence study was done according to the procedure of Celik et al. (2008) and the results were validated against experimental data with good agreement. The volume mesh contains approximately 14.2M elements with triangular prisms in the boundary layer of the blades and struts, and tetrahedral elements elsewhere. The maximum element length on the outer domain is $D/20$. The height of the first element in the boundary layer is 0.45mm and a total of ten layers with a 1.2 growth ratio are used. A time step of 1×10^{-4} s is used resulting in a maximum CFL number less than 10. As can be seen in Fig. 3.5, the mesh resolution downstream of the turbine is not refined to resolve the wake. Instead, the wake is studied using a multi-domain technique as discussed in Section 3.3.

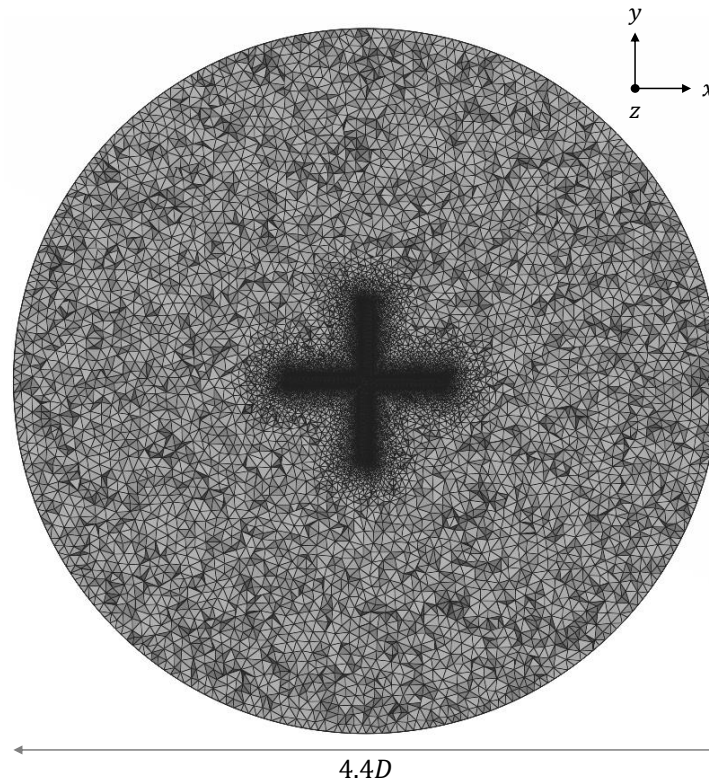


Figure 3.5: Slice of the computational mesh in the xy -plane for the tidal turbine.

3.2.2 Experimental validation

Figure 3.6 shows the instantaneous and mean power coefficient under a uniform inflow where the power coefficient is defined as $C_p = (T \Omega) / (0.5 \rho U_\infty^3 b D)$, where T is the torque generated by the turbine, Ω is the rotational speed of the

turbine, b is the blade span, and D is the rotor diameter. The mean power coefficient is compared to the experimental results provided by [New Energy Corporation](#) in Table 3.3 where the numerical power coefficient is averaged after two revolutions to allow the flow to develop. Note the experimental results correspond to full-scale field measurements at the same operating condition as that considered here. The experimental tests were performed in open water where the turbine was towed by a tugboat in a large circle to minimize wake effects from the boat. Future work is underway to improve the experimental results so that instantaneous comparisons and experimental uncertainties can be provided. Good agreement with the experimental results is found.

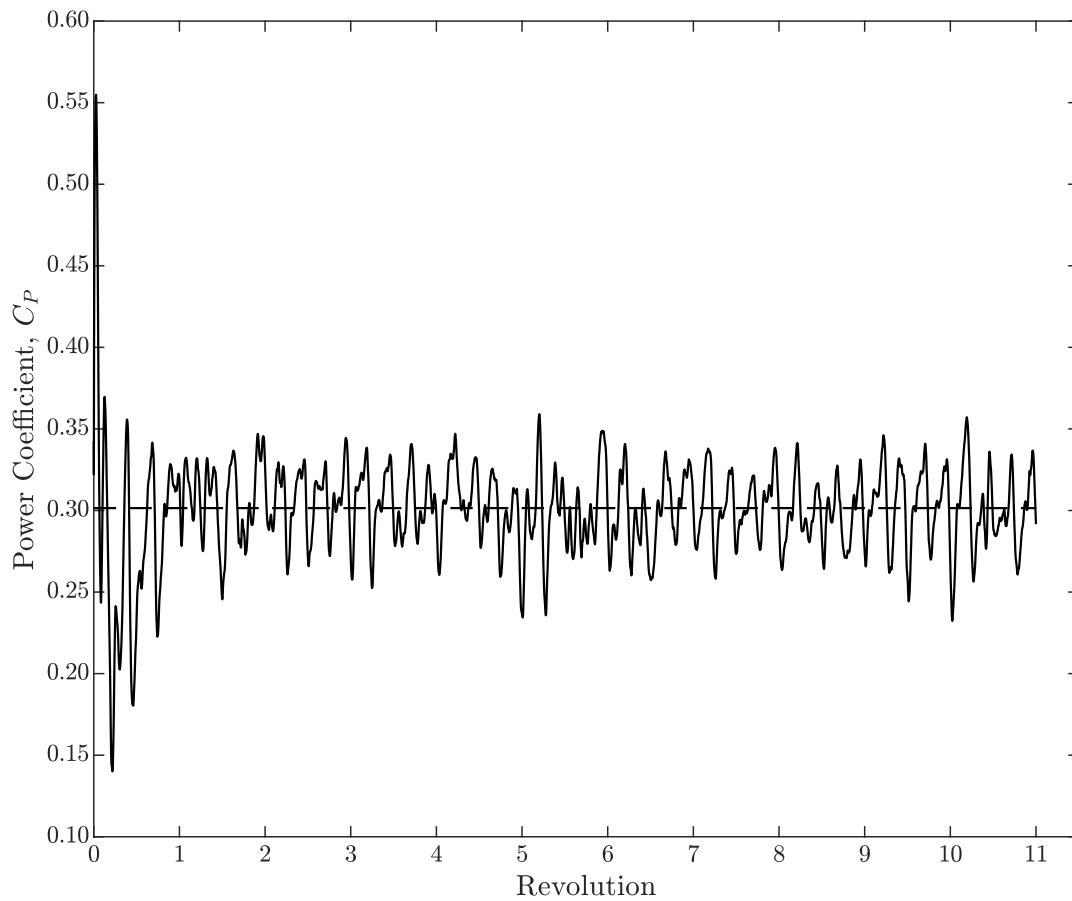


Figure 3.6: Instantaneous power coefficient under a uniform inflow (—) with the mean power coefficient (---) averaged after the first two revolutions.

Table 3.3: Comparison of power coefficient with experimental results.

	Power Coefficient, C_P	Percent Error (%)
Experimental	0.32	-
Numerical	0.30	6.3

3.2.3 Effect of a turbulent inflow on turbine performance

A comparison of the instantaneous power coefficient under a uniform and turbulent inflow is shown in Fig. 3.7. Under a uniform inflow, the mean power coefficient remains relatively constant with each revolution once the flow has developed. In contrast, there are large fluctuations present in the instantaneous power coefficient under a turbulent inflow likely due to interactions between the eddies in the flow field and the turbine.

The mean power coefficient and standard deviation of the power coefficient are shown in Table 3.4. In obtaining these quantities, the first two revolutions are omitted to allow the flow to develop. A turbulent inflow is found to slightly affect the mean power coefficient with a reduction of approximately 7-10%. A turbulent inflow is also found to increase the standard deviation of the power coefficient by a factor of approximately 2-2.5.

Similar findings are observed in numerical studies involving horizontal-axis turbines. In (Togneri et al., 2020), a blade element momentum theory model is used with SEM and the von Kármán spectral method to investigate the effect of turbulence on the power coefficient of a three-bladed horizontal-axis turbine. With both synthetic turbulence generation methods, the standard deviation of the power coefficient increased with increasing turbulence intensity, while the mean power coefficient was not significantly affected. In (Ahmed et al., 2017; Afgan et al., 2013), fully-resolved simulations were done using RANS and LES, respectively, to study the loading of a horizontal-axis turbine under a turbulent inflow that was generated using SEM. In (Afgan et al., 2013), the root mean square of the power coefficient was found to gradually increase with an increasing turbulence intensity, while the mean power coefficient was not significantly affected at the tip speed ratios considered in (Afgan et al., 2013). In contrast, a turbulent inflow resulted in a larger power coefficient for the operating condition considered in (Ahmed et al., 2017). This suggests that, at certain tip speed ratios, the effects of a turbulent inflow may be more significant on the performance of the turbine. In the context of vertical-axis tidal turbines, there are some experimental studies that investigate the effect of turbulence on the performance of the turbine. The effect of turbulence intensity on the performance of a Gorlov Helical turbine was studied by Bachant and Wosnik (2011). Under a turbulent inflow, the mean power coefficient was slightly smaller at higher tip speed ratios and slightly larger at lower tip speed ratios. The performance of full-scale turbines in real-sea conditions has also been studied although these studies are scarce. In Sentchev et al. (2020), the power production of a full-scale four-bladed H-Darrieus vertical-axis tidal turbine under real-sea conditions is investigated.

The fluctuations of the power generated increased when the flow became more turbulent. Moreover, the magnitude of the power fluctuations was found to increase with the integral length scale.

In the context of tidal turbine installations in real-site conditions, the results obtained provide some practical findings. As the mean power coefficient is similar for both turbulent inflow conditions, it may be possible to install turbines in sites with different levels of turbulence without a significant difference in the performance of the turbine. The increase in the standard deviation of the power coefficient under a turbulent inflow may necessitate more robust turbine designs as the fatigue life of the blades, generator, and gear box will be reduced.

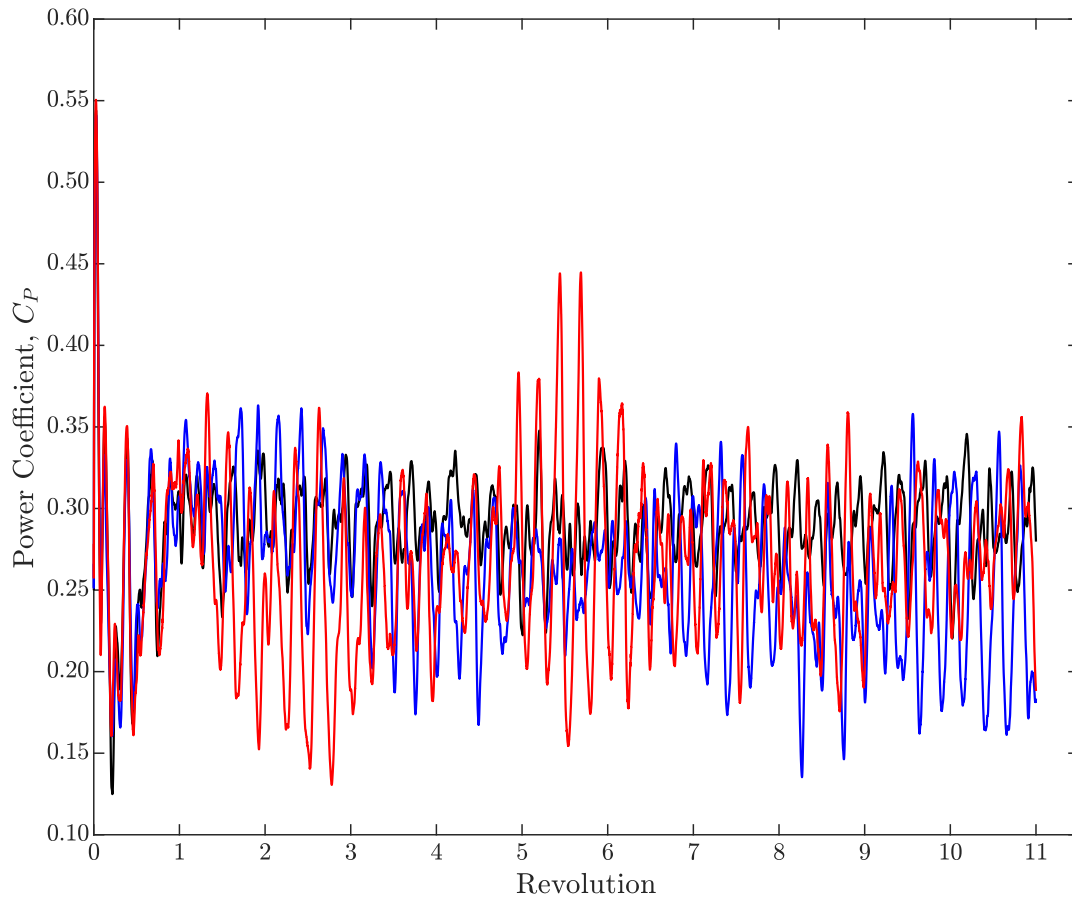


Figure 3.7: Instantaneous power coefficient under a uniform inflow (—) and turbulent inflow with 5% (—) and 10% (—) turbulence intensity.

Table 3.4: Comparison of mean power coefficient and standard deviation of power coefficient under a uniform and turbulent inflow.

Inflow	Power Coefficient, C_p	Standard Deviation, σ_{C_p}
Uniform	0.30	0.02
$T_i = 5\%$	0.27	0.04
$T_i = 10\%$	0.28	0.05

3.3 Near-wake characteristics of the turbine

3.3.1 Computational setup

The near-wake characteristics of the turbine are studied using the multi-domain method proposed in [Osawa et al. \(1999\)](#). This method consists of extracting the velocity field from a suitable plane in the main simulation and using this velocity field as a time-dependent inlet boundary condition for a secondary domain. In the present study, the velocity field is extracted at the right-most edge of the turbine rotor every 200 time steps (or 0.02s) and used as the inflow for the mesh shown in [Fig. 3.8](#). The velocity field is extracted after three turbine revolutions to allow the wake to develop. To interpolate the extracted velocity field from the main domain to the inlet of the secondary domain, the finite element shape functions are used. The width and height of the secondary domain is $4.3D$ and $2.4D$, respectively, and the length is $5D$. The volume mesh of the secondary domain consists of approximately 6.3M elements.

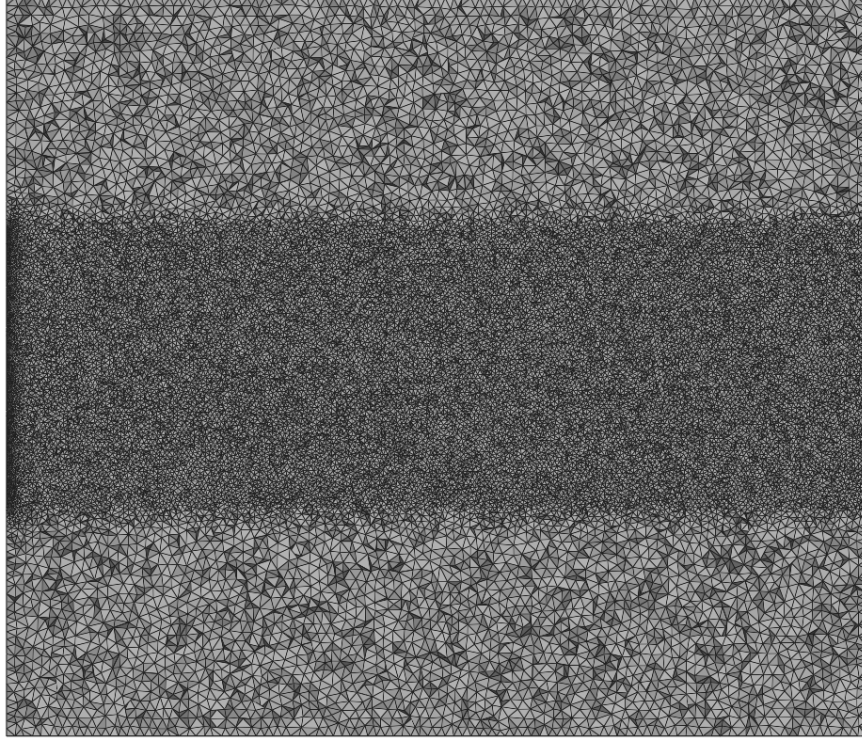


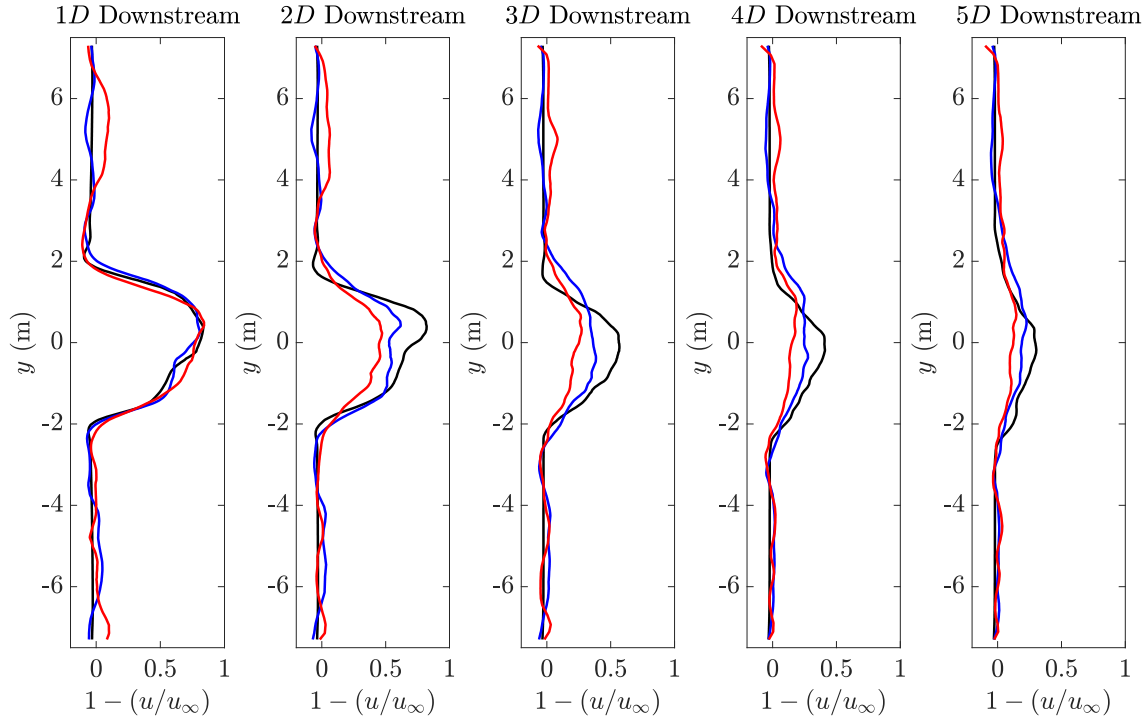
Figure 3.8: Slice of the computational mesh in the xy -plane for the secondary domain.

3.3.2 Near-wake characteristics under a uniform and turbulent inflow

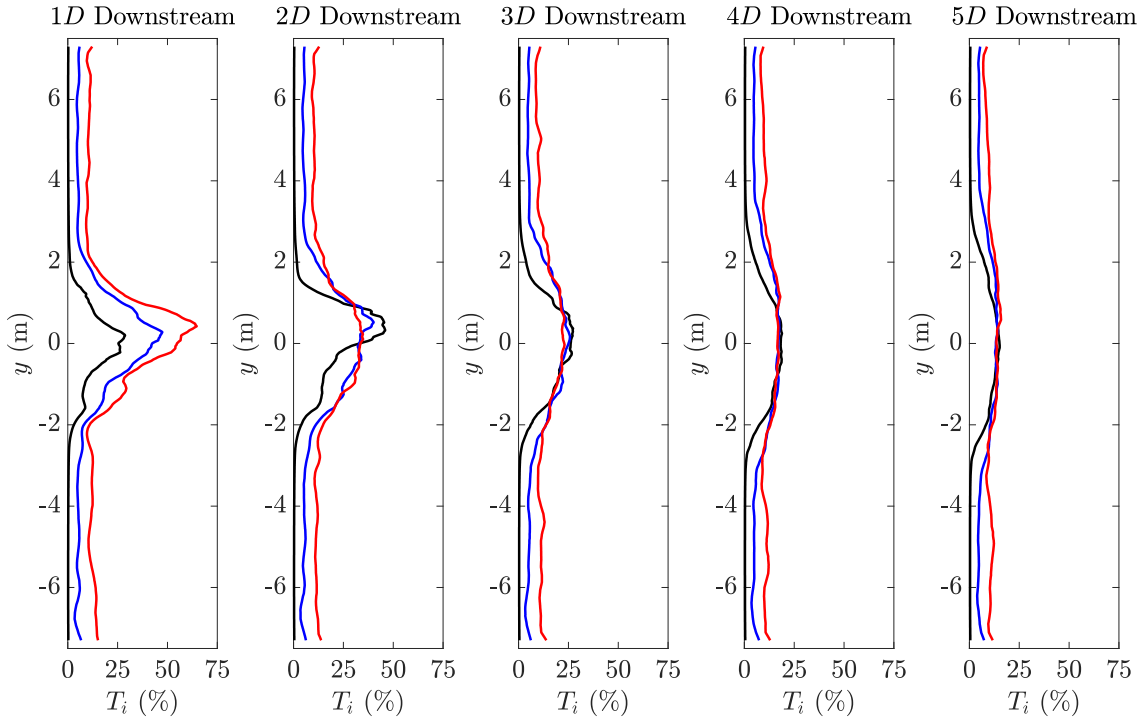
The velocity deficit and turbulence intensity in the wake of the turbine is shown in Fig. 3.9. These results are obtained in the xy -plane at the midpoint of the turbine blades. Note that the velocity deficit is defined as $1 - (u/u_\infty)$. As can be seen in Fig. 3.9a, a higher incoming turbulence intensity leads to a quicker recovery of the velocity deficit. An improvement of the velocity deficit recovery can be seen clearly at $2D$ downstream of the turbine. While the maximum velocity deficit from $1D$ to $2D$ downstream reduces by only 2% under a uniform inflow, it reduces by 23% and 44% under a turbulent inflow with $T_i = 5\%$ and $T_i = 10\%$, respectively. At $5D$ downstream of the turbine, the maximum velocity deficit under a turbulent inflow with $T_i = 5\%$ and $T_i = 10\%$ is 0.23 and 0.15, respectively, while it is 0.30 under a uniform inflow.

The shape of the velocity deficit profile is also affected by a turbulent inflow. At $1D$ downstream of the turbine, an asymmetry between $y > 0$ and $y < 0$ exists for each case as the blades extract more energy from the flow at $y > 0$ where the blades rotate into the incoming flow. The shape of the velocity deficit profiles at $1D$ downstream are similar for each inflow condition with slightly less asymmetry at the center of the profile for a turbulent inflow with $T_i = 10\%$. Moreover, the asymmetry in the center of the profile quickly becomes less evident under a turbulent inflow as the wake expands in the lateral direction where $y > 0$. Under a uniform inflow, the asymmetry at the center of the profile persists until approximately $3D$ downstream of the turbine.

The turbulence intensity downstream of the turbine is shown in Fig. 3.9b. Similar to the velocity deficit profiles in Fig. 3.9a, the turbulence intensity profiles are asymmetric with the maximum turbulence intensity occurring at $y > 0$. Moreover, the turbulence intensity recovers to the ambient turbulence intensity at a quicker rate under a more turbulent inflow. At $5D$ downstream of the turbine, the maximum turbulence intensity is $2.8\times$ and $1.6\times$ larger than the ambient turbulence intensity under a turbulent inflow with $T_i = 5\%$ and $T_i = 10\%$, respectively. In contrast, the maximum turbulence intensity under a uniform inflow at $5D$ downstream of the turbine is comparable to the intensity under both turbulent inflows indicating a slower wake recovery for the uniform inflow. It is interesting to note the differences in the downstream location of the maximum turbulence intensity for each inflow condition. Under a turbulent inflow, the maximum turbulence intensity occurs approximately $1D$ downstream of the turbine, whereas under a uniform inflow, the maximum turbulence intensity occurs approximately $2D$ downstream of the turbine. A connection can be drawn between the location of the maximum turbulence intensity and the asymmetry in the velocity deficit profile. At locations downstream of the maximum turbulence intensity, the asymmetry in the center of the velocity deficit profile is less evident.



(a) Velocity deficit.



(b) Turbulence intensity.

Figure 3.9: Time-averaged velocity deficit and turbulence intensity in the wake of the turbine under a uniform inflow (—) and turbulent inflow with 5% (—) and 10% (—) turbulence intensity. Results are obtained in the xy -plane at the midpoint of the turbine blades.

To visualize the shape of the velocity profile and the mixing of flow structures in the wake of the turbine, the time-averaged streamwise velocity field and instantaneous vorticity field in the z -direction are shown in Fig. 3.10. Once again, the improvement in the wake recovery with an increasingly turbulent inflow can be seen. Moreover, the asymmetry of the wake is also seen to persist to a farther downstream distance under a uniform inflow. As the inflow becomes more turbulent, this asymmetry becomes less evident at an earlier downstream distance. The mixing of the flow structures can be visualized by the instantaneous vorticity field. Under a uniform inflow, the flow structures begin interacting strongly farther downstream compared to a turbulent inflow, where the mixing is also more significant. Moreover, the location where the flow structures interact most significantly coincides with the location of the rapid recovery of the velocity deficit. The labels, A and B, in Fig. 3.10 refer to the vortices shed by the turbine and the vortices of the ambient flow, respectively. As expected, there are no vortices in the ambient flow under a uniform inflow.

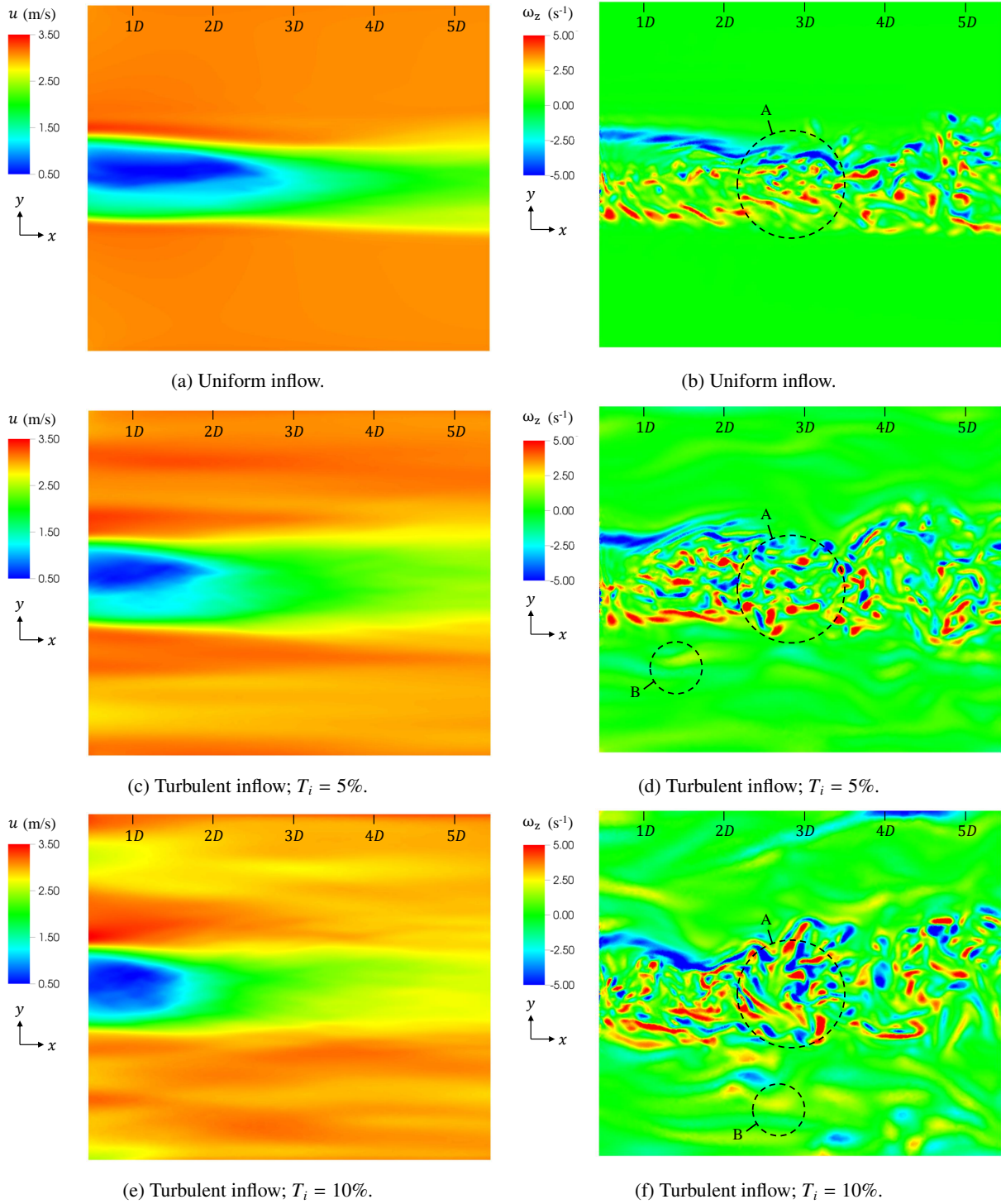
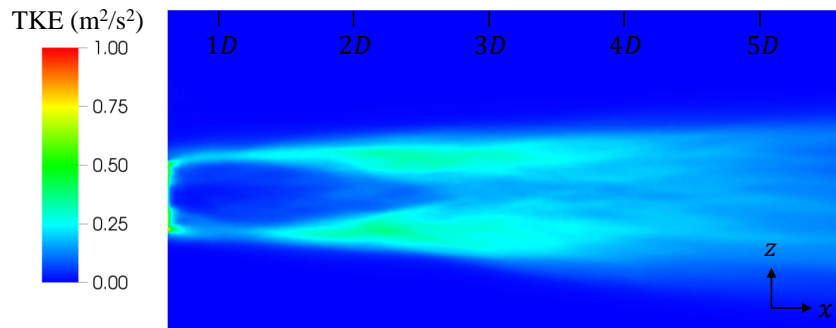


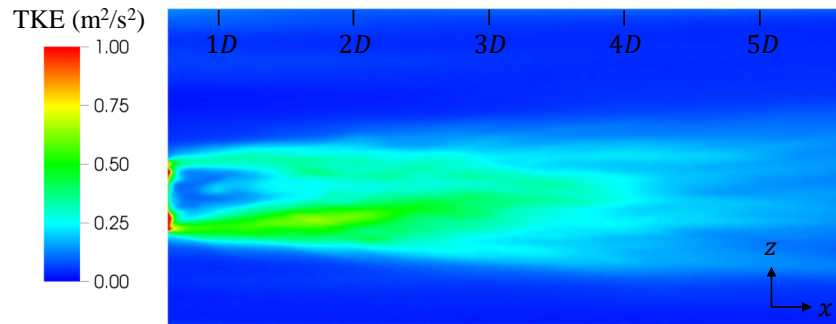
Figure 3.10: Time-averaged streamwise velocity field (left) and instantaneous vorticity component in the z -direction (right) in the wake of the turbine under different inflow conditions. Slice is taken in the xy -plane at the midpoint of the turbine blades. Note the origin is at the turbine shaft.

A slice of the turbulent kinetic energy (TKE) in the xz -plane at the center of the turbine is shown in Fig. 3.11. It can be seen that under an increasingly turbulent inflow, the blade tip vortices above and below the turbine begin

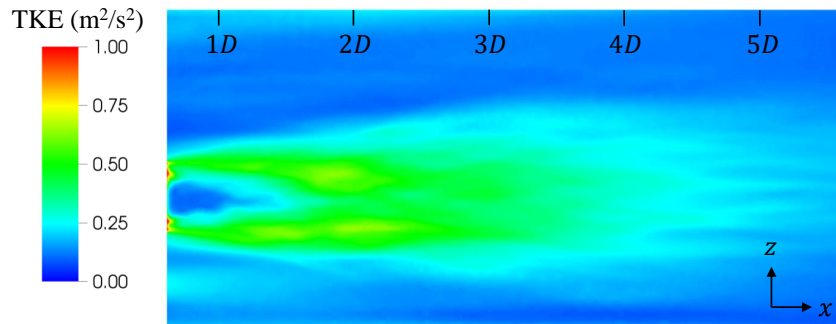
interacting at an earlier downstream distance. This observation is consistent with the improved wake recovery under a turbulent inflow that was observed in Figs. 3.9 and 3.10. Moreover, the TKE expands more in the vertical direction as the inflow becomes more turbulent. To visualize the flow structures in the wake of the turbine, the instantaneous vorticity isovolumes colored by the velocity magnitude are shown in Fig. 3.12. Note that the isovolumes outside the turbine rotor diameter are omitted to focus on the interaction directly behind the turbine. It can be seen that under a uniform inflow, the flow structures remain coherent until approximately $2.5D$ after which they mix strongly with each other. In contrast, under a turbulent inflow, the flow structures appear to break down almost immediately and the improved mixing leads to a quicker wake recovery.



(a) Uniform inflow.



(b) Turbulent inflow; $T_i = 5\%$.



(c) Turbulent inflow; $T_i = 10\%$.

Figure 3.11: Time-averaged turbulent kinetic energy (TKE) in the wake of the turbine under different inflow conditions. Slice is taken in the xz -plane through the center of the turbine. Note the origin is at the turbine shaft.

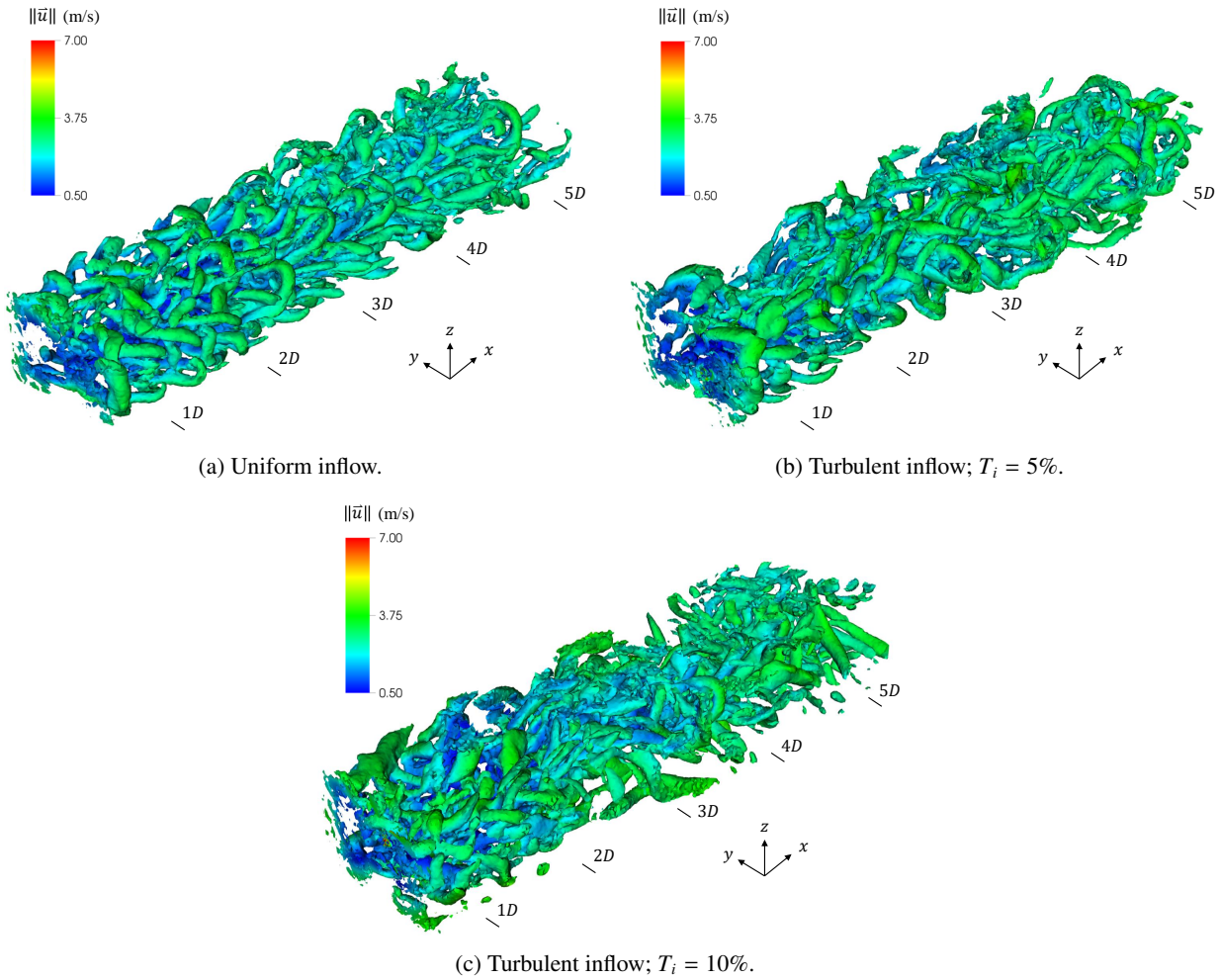


Figure 3.12: Instantaneous vorticity isovolumes colored by velocity magnitude in the wake of the turbine under different inflow conditions. Note the origin is at the turbine shaft.

A turbulent inflow is found to have a notable effect on the recovery of the turbine wake. These results are important to consider when designing a tidal array, where downstream turbines are influenced by the wake of upstream turbines. As the wake recovery is improved under a turbulent inflow, it may be possible to use a smaller streamwise inter-device spacing in tidal sites with a notable degree of turbulence leading to a smaller footprint.

Chapter 4

Effect of a free surface and different blade-strut configurations on a vertical-axis tidal turbine

In this chapter, the effect of a free surface and different blade-strut configurations on a vertical-axis tidal turbine is studied. In Sections 4.2 and 4.3, the effect of a free surface on the performance of two blade-strut configurations is studied. A case of deep immersion and shallow immersion is considered for each blade-strut configuration. Moreover, the effect of immersion depth on free-surface deformation and turbine performance is discussed. In Section 4.4, differences in the near-wake characteristics are discussed for each case.

4.1 Computational setup

The first turbine configuration studied in this work is designed and manufactured by [New Energy Corporation](#) and is shown in Fig. 4.1a. It is a 25kW four-bladed H-Darrieus vertical-axis tidal turbine with the struts located at the quarter-span position of the blades. The geometric parameters of the turbine are summarized in Table 4.1. The operating condition, provided by [New Energy Corporation](#), consists of a mean inflow velocity (U_∞) of 3.0 m/s and a rotational speed of the turbine (Ω) of 3.67 rad/s. The tip speed ratio of the turbine, defined as $\lambda = (0.5 \Omega D)/U_\infty$ is 2.08. The second blade-strut configuration studied is shown in Fig. 4.1b. This configuration was chosen based on the results reported by [Villeneuve et al. \(2021\)](#). From all the configurations simulated by [Villeneuve et al. \(2021\)](#), the turbine with struts located at the blade-tips with a curvature radius of $R' = 0.5c$ was the most efficient. As can be seen in Fig. 4.1b, the shaft height for the tip-struts configuration was increased at the bottom of the shaft since, in a

complete design, a hub is installed to which the struts are bolted to.

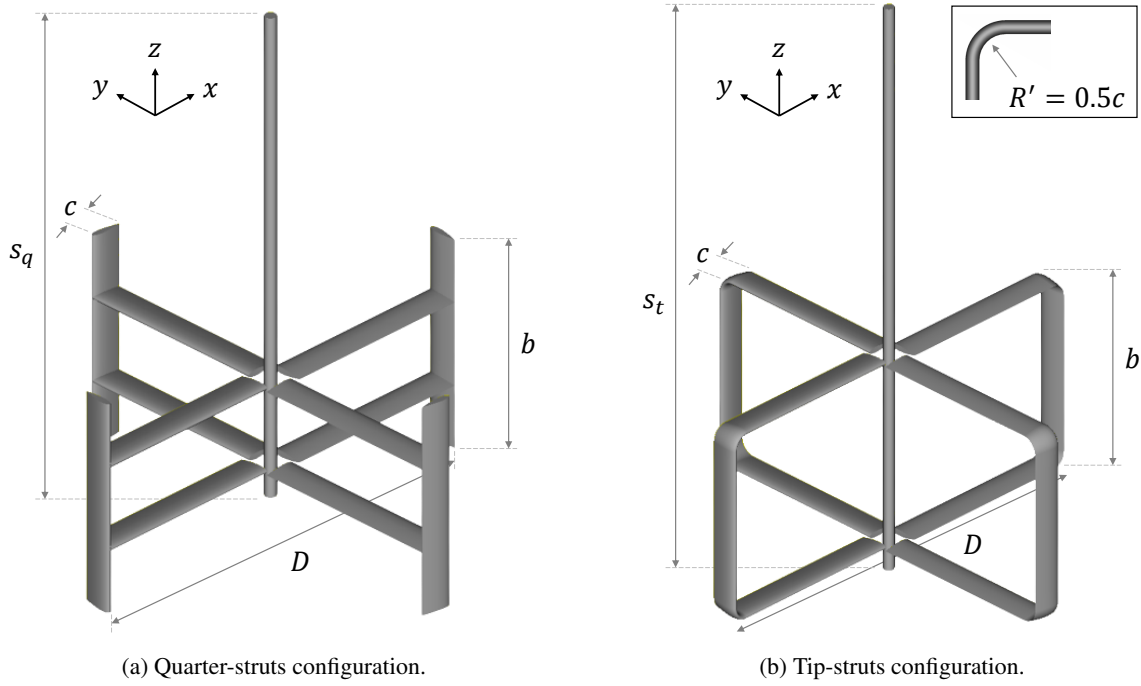


Figure 4.1: Geometry of 25kW tidal turbine. The dimensions of the geometric parameters are listed in Table 4.1.

Table 4.1: Geometric parameters of 25kW tidal turbine.

Parameter	Value
Blade/Strut Profile	NACA 0021
Rotor Diameter (D)	3.4m
Blade Span (b)	1.7m
Quarter-struts Shaft Height (s_q)	4.7m
Tip-struts Shaft Height (s_t)	6.0m
Chord Length (c)	0.254m
Aspect Ratio (b/c)	6.7

A slice of the computational domain in the xy -plane is shown in Fig. 4.2. An ALE description of the continuum is used to allow the domain to rotate at the rotational speed of the turbine while the flow field is captured using an Eulerian description. The left-hand side of the cylindrical domain boundary is treated as the inlet, while the right-hand side is treated as the outlet. A uniform velocity field is prescribed at the inlet, while a traction-free boundary condition

is naturally satisfied at the outlet. A no-penetration boundary condition is prescribed at the top and bottom boundaries of the cylindrical domain. The no-slip boundary condition is imposed weakly on the blades, struts, and shaft such that the flow velocity and mesh velocity are equal on these surfaces. In the air portion of the domain, the air velocity is set to zero. Moreover, the level-set function is prescribed at the domain inlet by a signed distance function depending on the desired inlet water level.

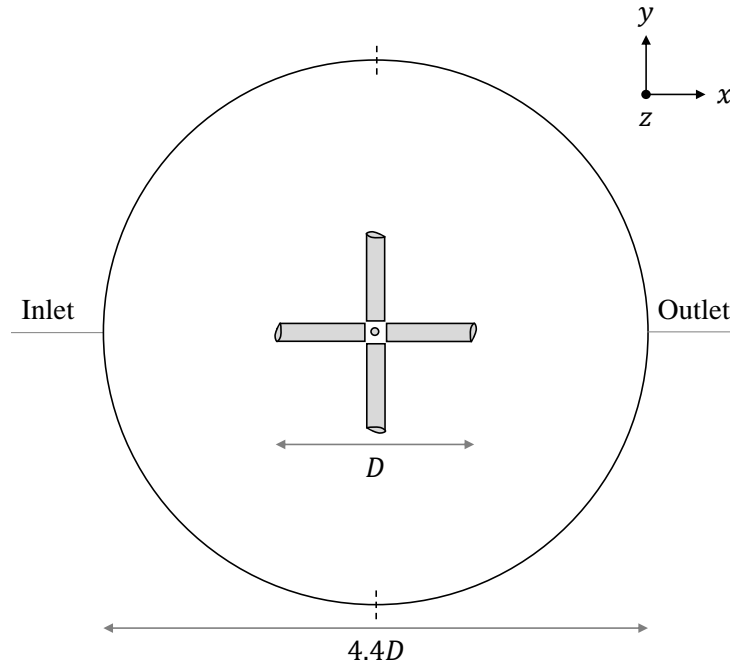


Figure 4.2: Computational domain of turbine in the xy -plane (not to scale).

Two distances h between the blade tips and free surface are considered corresponding to a deep immersion case where $h = 0.8D$ and a shallow immersion case where $h = 0.1D$. A slice of the mesh in the xz -plane for the tip-struts configuration under deep immersion is shown in Fig. 4.3. A similar mesh is built for the quarter-struts configuration. Note that additional mesh refinement is applied near the free surface. For the shallow immersion case, the free-surface refinement region is translated downwards. All volume meshes contain approximately 25-28M elements with triangular prisms in the boundary layer of the blades and struts, and tetrahedral elements elsewhere. A time step of 1×10^{-4} s is used for each case resulting in a maximum CFL number less than 10.

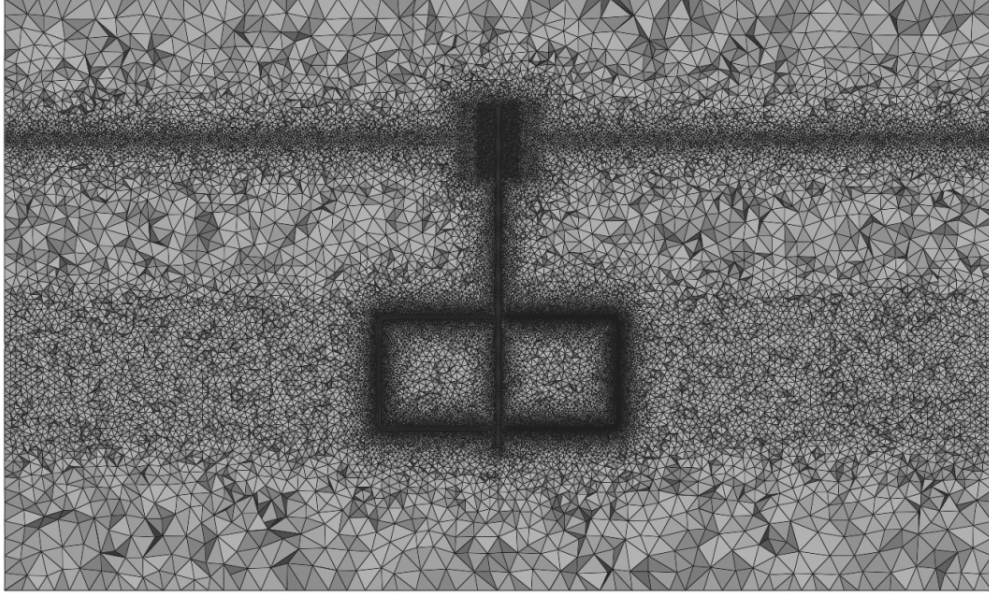


Figure 4.3: Slice of the computational mesh in the xz -plane for the tip-struts configuration with a deep-immersion depth of $h = 0.8D$.

4.2 Performance comparison of quarter-struts and tip-struts designs under deep immersion

The performance of each blade-strut configuration was first studied under a deep immersion depth of $h = 0.8D$. Figures 4.4 and 4.5 show the power coefficient defined as $C_p = (T \Omega) / (0.5 \rho U_\infty^3 b D)$, where T is the torque generated by the turbine, for each configuration. Table 4.2 shows the mean power coefficient for each case.

For the quarter-struts configuration, the mean power coefficient under deep immersion is compared to the mean power coefficient with no free surface and to the experimental results provided by [New Energy Corporation](#). Note that the experimental results correspond to full-scale field measurements at the same operating condition as that considered here. While some differences in the instantaneous power coefficient between the deep-immersion case and no free-surface case can be seen in Fig. 4.4, there is no effect on the mean power coefficient as seen in Table 4.2. This suggests that a free surface has a negligible effect on the performance of a deeply-immersed turbine.

The performance of the quarter-struts configuration was compared to the tip-struts configuration under the same deep immersion depth of $h = 0.8D$. It can be seen from Table 4.2 that the tip-struts configuration is 15% more efficient than the quarter-struts configuration. The improvement in efficiency of the tip-struts configuration is consistent with the results of [Marsh et al. \(2015c\)](#) and [Villeneuve et al. \(2021\)](#). Although the improvement in efficiency is not as significant as that reported by [Villeneuve et al. \(2021\)](#), it is important to note that their study considered a single-blade turbine. The improvement in efficiency is more comparable to the results of [Marsh et al. \(2015c\)](#) although no curvature

radius was used for the tip-struts configuration by [Marsh et al. \(2015c\)](#). It was suggested by [Villeneuve et al. \(2021\)](#) that the struts in the tip-struts configuration act to reduce the induced drag component on the blade section. It is important to note that the present study only considers a single tip speed ratio. Therefore, the performance difference between each blade-strut configuration may be different at different tip speed ratios.

4.3 Effect of shallow immersion on free-surface deformation and turbine performance

The effect of a shallow immersion depth of $h = 0.1D$ on free-surface deformation and the performance of each blade-strut configuration was studied next. To visualize the free-surface deformation, the free surface along with the instantaneous vorticity isovolumes colored by the velocity magnitude are shown in [Fig. 4.7](#).

For both blade-strut configurations, there is a clear effect on the free surface when a shallow immersion depth is considered. Under deep immersion, there is a negligible effect of the turbine wake on the free surface. Instead, the free surface is primarily affected by the vortex shedding downstream of the shaft. For the shallow-immersion case, the free-surface deformation increases significantly due to interactions between the turbine wake and free surface. Moreover, the height of the free surface slightly rises upstream of the turbine and falls through the turbine as energy is extracted from the flow ([Consul et al., 2013](#)).

A difference in the free-surface deformation between each blade-strut configuration can also be observed. As found in ([Villeneuve et al., 2021](#); [Villeneuve and Dumas, 2021](#)), the blade-tip vortices are affected by a rounded blade-strut junction. It was reported by [Villeneuve and Dumas \(2021\)](#) that the vorticity distribution at the blade tips is spread out over the blade and struts when a rounded junction is used which reduces the vertical velocity component induced in the near-wake. This finding is consistent with the free-surface deformation observed in [Fig. 4.7](#) where, under shallow immersion, the free-surface deformation is more significant for the quarter-struts configuration compared to the tip-struts configuration.

In addition to differences in the free-surface deformation, there are also differences in the performance of each blade-strut configuration under shallow immersion. The performance of both turbine designs reduced under a shallow immersion depth due to interactions between the turbine wake and free surface as is consistent with other studies ([Bahaj et al., 2007](#); [Kolekar and Banerjee, 2015](#)). It is interesting to note from [Table 4.2](#) that the performance of the quarter-struts configuration was more significantly affected with a performance reduction of 6% compared to the deep-immersion case. Alternatively, the performance of the tip-struts configuration only reduced by 2%. This performance difference may be explained by considering the differences in the free-surface deformation under a shallow immersion for each configuration. As there is less interaction between the free surface and turbine wake of the tip-

struts configuration due to the rounded blade-strut junction, it may be expected that the performance is affected less significantly.

4.4 Differences in the near-wake characteristics

Although the purpose of the current study is not to extensively study the wake, it is worth discussing differences in the near-wake characteristics for each case. For this purpose, the instantaneous streamwise velocity field and the phase-averaged velocity deficit curves in the xz -plane at the center of the domain are shown in Figs. 4.6 and 4.8, respectively. Note that in Fig. 4.8, the velocity deficit is defined as $1 - (u/u_\infty)$, where u/u_∞ is the ratio between the streamwise velocity and the freestream velocity, and the range of the vertical axis is from the bottom of the domain to the specified water level.

It can be seen from Figs. 4.6 and 4.8 that under deep immersion, the maximum velocity deficit is slightly greater for the tip-struts configuration at $1D$ downstream of the turbine. Moreover, the extent of the velocity deficit is larger for the tip-struts configuration compared to the quarter-struts configuration at this downstream distance. For the tip-struts configuration, the location of the two largest velocity deficits are near the blade-tips where the struts are placed. Alternatively, the peak velocity deficit of the quarter-struts configuration is located near the center of the blade. At $2D$ downstream of the turbine, the velocity deficit of both configurations are similar, but it can be noted in Fig. 4.6 that the wake of the quarter-struts configuration expands noticeably in the vertical direction while the size of the wake of the tip-struts configuration remains fairly consistent.

Similar observations can be made about the velocity deficit under shallow immersion. The peak velocity deficit of the tip-struts configuration is once again larger than the quarter-struts configuration. Unlike the deep immersion case where the velocity deficit curves for both configurations are similar at $2D$ downstream of the turbine, the extent and magnitudes of the velocity deficit are noticeably larger for the tip-struts configuration than the quarter-struts configuration under shallow immersion. The differences in strut position are clearly reflected in the velocity deficit curves under shallow immersion at $2D$ downstream of the turbine. Once again, the two largest velocity deficits of the tip-struts configuration correspond to the location of the struts at the blade tips while the peak velocity deficit of the quarter-struts configuration is near the center of the blade. Moreover, the shape of both curves is more symmetrical compared to the deep immersion case as the wake of the shaft is negligible under shallow immersion.

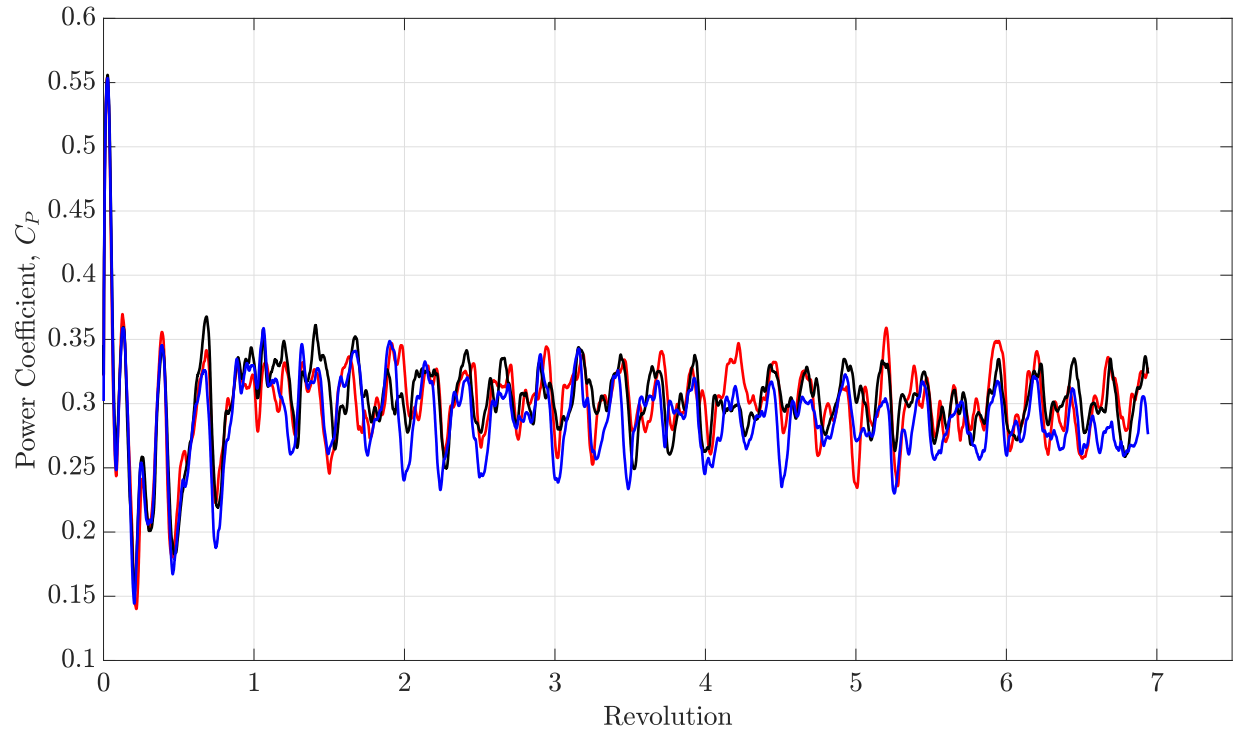


Figure 4.4: Instantaneous power coefficient for quarter-struts configuration under different conditions. Lines are colored as follows: quarter-struts under deep immersion (—), quarter-struts under shallow immersion (—), and quarter-struts with no free surface (—). Deep and shallow immersion corresponds to $h = 0.8D$ and $h = 0.1D$, respectively.

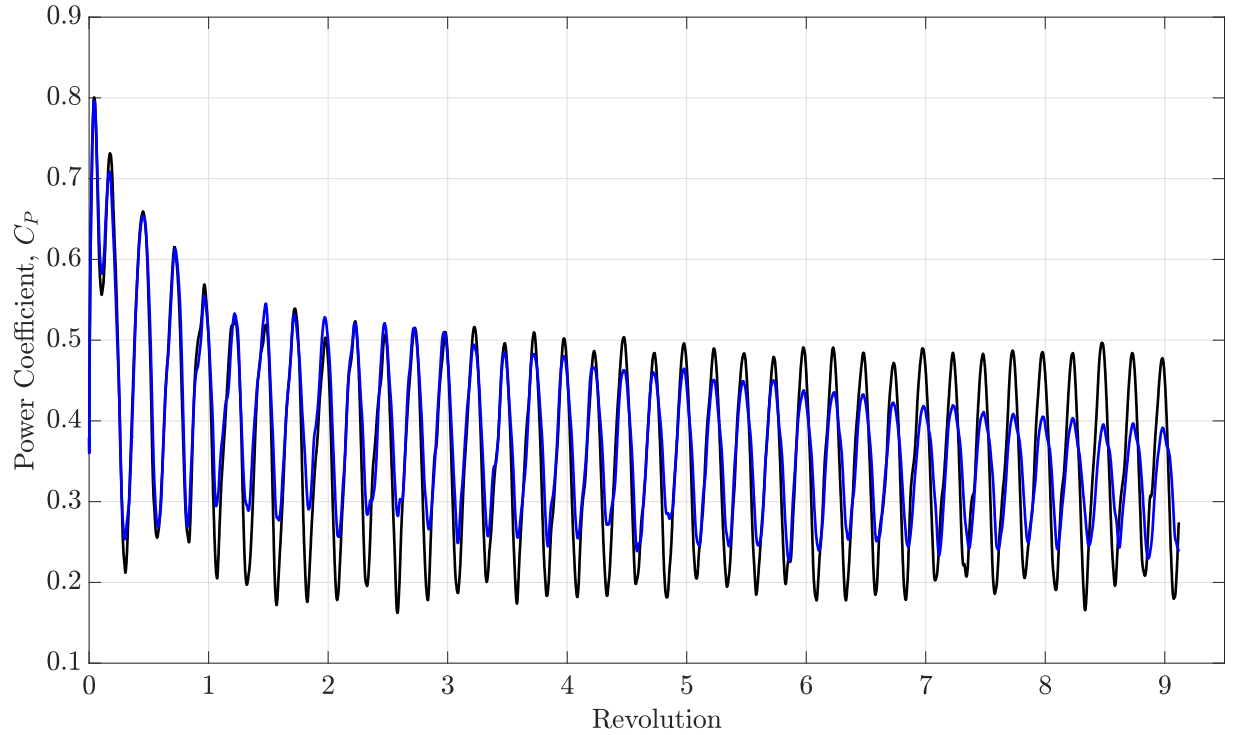


Figure 4.5: Instantaneous power coefficient for tip-struts configuration under different conditions. Lines are colored as follows: tip-struts under deep immersion (—) and tip-struts under shallow immersion (—). Deep and shallow immersion corresponds to $h = 0.8D$ and $h = 0.1D$, respectively.

Table 4.2: Power coefficient of each blade-strut configuration under different conditions.

Configuration	Case	Power coefficient, C_P
Quarter-struts	Experimental	0.320
	No free surface	0.301
	Deep immersion; $h = 0.8D$	0.301
	Shallow immersion; $h = 0.1D$	0.282
Tip-struts	Deep immersion; $h = 0.8D$	0.344
	Shallow immersion; $h = 0.1D$	0.337

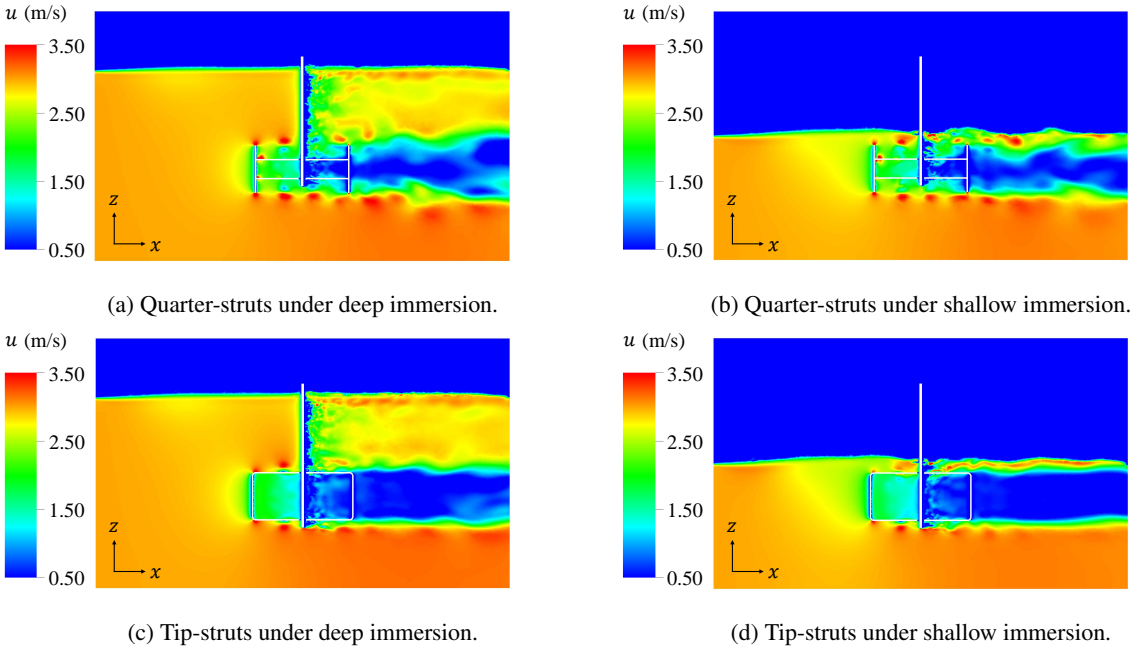


Figure 4.6: Instantaneous streamwise velocity field in the xz -plane for each blade-strut configuration under deep immersion ($h = 0.8D$) and shallow immersion ($h = 0.1D$).

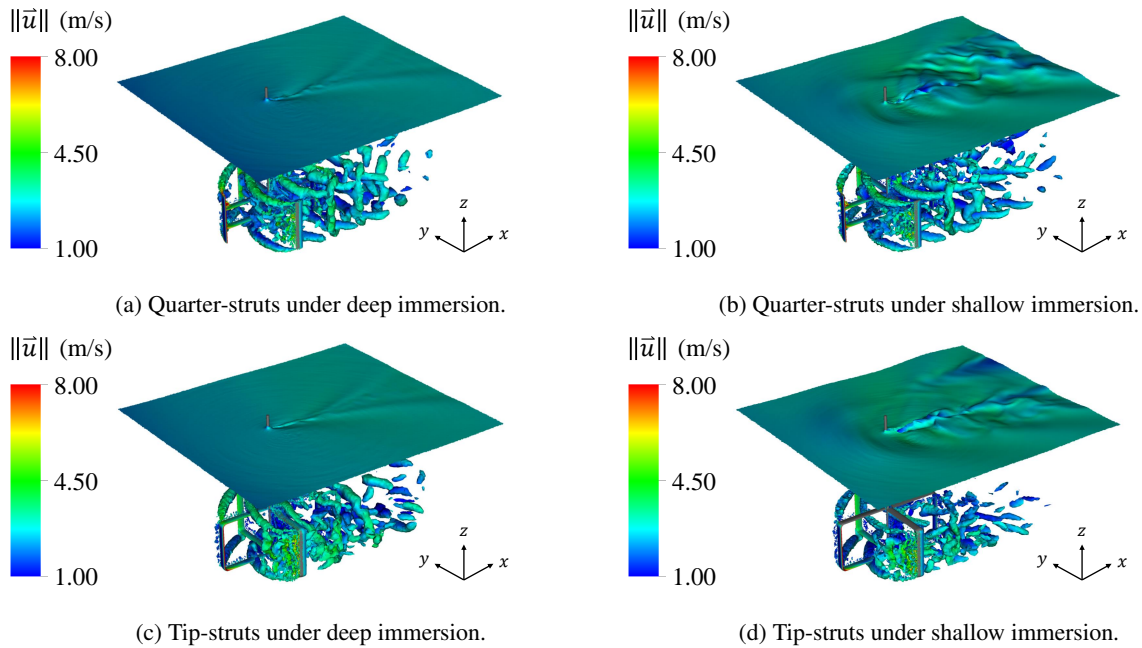
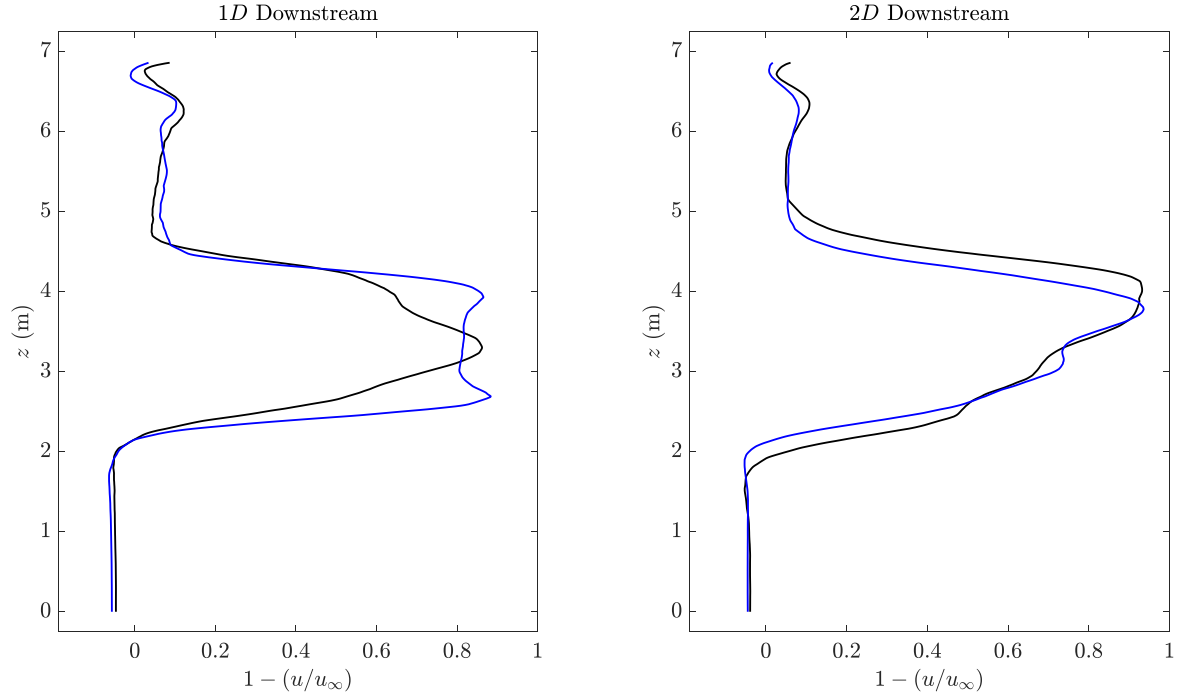
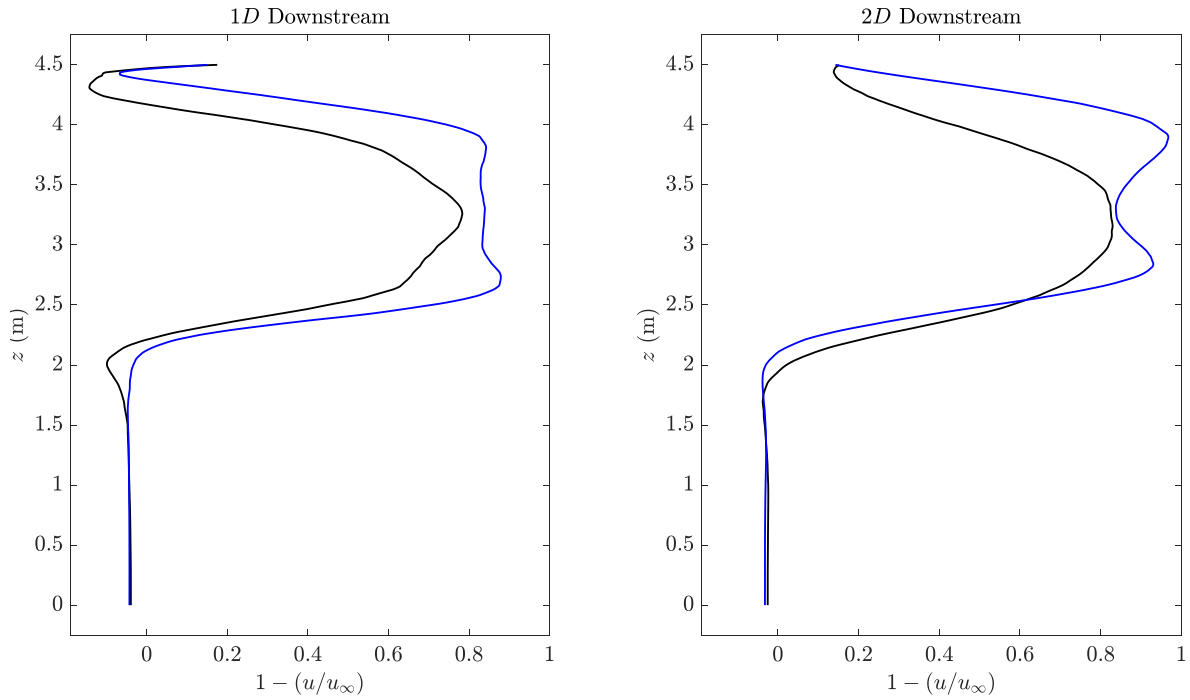


Figure 4.7: Free surface and instantaneous vorticity isovolumes colored by velocity magnitude for each blade-strut configuration under deep immersion ($h = 0.8D$) and shallow immersion ($h = 0.1D$). Note that for the shallow immersion cases, the free surface has been translated upwards during visualization to keep the same view as the deep immersion cases.



(a) Deep immersion.



(b) Shallow immersion.

Figure 4.8: Phase-averaged velocity deficit in the wake of the turbine under deep immersion and shallow immersion for the quarter-struts (—) and tip-struts (—) configuration. Results are obtained in the xz -plane at the center of the domain. Note the origin is at the turbine shaft.

Chapter 5

Conclusions

5.1 Effect of turbulence on tidal turbines

This thesis first investigated the effect of a turbulent inflow on the performance and wake of a four-bladed vertical-axis tidal turbine using the arbitrary Lagrangian-Eulerian variational multiscale (ALE-VMS) formulation. A uniform inflow and turbulent inflow with a 5% and 10% turbulence intensity was considered where the turbulent inflow was generated using Smirnov's random flow generation (RFG) method. The ALE-VMS formulation was augmented with a weak imposition of the Dirichlet boundary condition to relax the mesh resolution requirements at no-slip surfaces. Moreover, the wake was studied using a multi-domain technique to reduce the computational requirements of the main simulation.

Using VMS instead of classical LES eliminates any challenges with specifying an appropriate filter for different flows. Moreover, with the residual-based variational multiscale formulation, traditional eddy viscosities that are used to represent turbulent dissipation are not introduced. From the numerous synthetic turbulence generation methods available, Smirnov's RFG was chosen as it can generate a turbulent velocity field that is divergence-free for the case of homogeneous turbulence. A divergence-free velocity field ensures compatibility with the incompressible Navier-Stokes equations that govern the flow field.

The implementation of Smirnov's RFG method in the ALE-VMS framework was first validated by simulating a turbulent flow over a rectangular cylinder with a 5:1 aspect ratio. This case is referred to as a benchmark on the aerodynamics of a rectangular 5:1 cylinder (BARC). The pressure coefficient and root mean square of the pressure coefficient over the top-half of the central section of the rectangular cylinder was compared to the numerical results of [Ricci et al. \(2017\)](#) and experimental results of [Mannini et al. \(2017\)](#) with good agreement. Prior to studying the effect of a turbulent inflow on the performance of the tidal turbine, the mean power coefficient under a uniform inflow was

validated against the experimental results provided by [New Energy Corporation](#).

The effect of a turbulent inflow on the performance of the turbine was first studied. A turbulent inflow was found to produce large fluctuations in the instantaneous power coefficient which are likely caused by interactions between the eddies in the flow field and the turbine. The mean power coefficient was found to be approximately 7-10% lower under a turbulent inflow compared to a uniform inflow. A negligible difference in the mean power coefficient was found between the two turbulent inflows of 5% and 10% turbulence intensity. Along with the mean power coefficient, the standard deviation of the power coefficient was also investigated and found to be 2-2.5× larger under a turbulent inflow.

To study the effect of a turbulent inflow on near-wake characteristics, a multi-domain method was used. The velocity field was extracted from a suitable plane in the main simulation and used as a time-dependent inlet boundary condition for a secondary domain. A turbulent inflow was found to result in a quicker recovery of the velocity deficit. Moreover, the turbulence intensity recovered to the ambient turbulence intensity more quickly under a turbulent inflow. Upon examining the instantaneous vorticity isovolumes, it was found that the flow structures remain coherent until a farther downstream distance under a uniform inflow. In contrast, under a turbulent inflow, they break down rapidly and the improved mixing leads to a quicker wake recovery.

The present study has certain useful implications in the context of tidal turbine installations in real-site conditions. Considering that the turbulence intensity at a tidal site may vary with time, the performance of the turbine should not be significantly affected if the mean velocity remains the same. While the mean power coefficient is not expected to be significantly affected by the turbulence intensity, a turbulent inflow may result in large fluctuations of the instantaneous power coefficient. This may necessitate more robust turbine designs as the fatigue life of the blades, generator, and gear box will be reduced. The degree of turbulence present in the tidal site is also important to consider when designing a tidal array. Namely, a shorter streamwise inter-device spacing may be acceptable in highly turbulent tidal sites.

For future work, this study can be extended to investigate the effect of a turbulent inflow on turbine performance and near-wake characteristics under different tip speed ratios (TSR). As only one TSR is considered in this study, such an investigation would be useful to verify if the findings of this study are the same at different tip speed ratios. Considering the turbulent inflow, it is useful to investigate the effect of different integral length scales of turbulence on the fluctuations of the power coefficient as it was reported by [Sentchev et al. \(2020\)](#) that the magnitude of the power fluctuations increased with an increasing integral length scale. Further research into this topic may enable more cost-effective turbine designs that are capable of handling the conditions at a specific tidal site. Moreover, it is worthwhile to examine if changes in the integral length scale affect the wake recovery to ensure that tidal arrays are designed effectively.

5.2 Effect of a free surface on tidal turbines

Next, this thesis investigated the effect of a free surface on the performance and flow field of a four-bladed vertical-axis tidal turbine with different blade-strut configurations. Numerical simulations were once again done using the ALE-VMS formulation. Two different blade-strut configurations were considered: quarter-struts and tip-struts with a rounded junction. For each blade-strut configuration, a deep immersion depth of $h = 0.8D$ and shallow immersion depth of $h = 0.1D$ was considered, where h is the distance between the blade-tips and free surface and D is the rotor diameter.

The performance of each blade-strut configuration was first studied under a deep immersion depth of $h = 0.8D$. The power coefficient of the quarter-struts configuration under deep immersion was compared to a case with no free surface. For both cases, the mean power coefficient was identical suggesting that a free surface has a negligible effect on the performance of a deeply-immersed turbine. The performance of each blade-strut configuration was also compared and the tip-struts configuration was 15% more efficient than the quarter-struts configuration under deep immersion.

A shallow immersion depth of $h = 0.1D$ was considered next to determine its effect on free-surface deformation and turbine performance. There was a clear effect on free-surface deformation under shallow immersion due to interactions between the turbine wake and free surface. Moreover, the free-surface deformation was less significant for the tip-struts configuration due to differences in the blade-tip vortices. As the vorticity distribution at the blade-tips is spread out over the blade and struts when a rounded junction is used, the vertical velocity component induced in the near-wake is reduced (Villeneuve and Dumas, 2021; Bachant and Wosnik, 2015). This reduces the free-surface deformation for the tip-struts configuration.

There were also differences in the performance of each blade-strut configuration under a shallow immersion depth. The performance of both turbine designs was less under shallow immersion compared to deep immersion due to interactions between the turbine wake and free surface. The performance of the quarter-struts configuration reduced by 6% while the performance of the tip-struts configuration reduced by 2%. As there is less interaction between the free surface and turbine wake of the tip-struts configuration, it may be expected that the performance is affected less significantly.

The present study has certain useful implications in the context of tidal turbines. As the performance of each blade-strut configuration reduced under shallow immersion, it may be advantageous to immerse turbines deeply enough to minimize interactions between the turbine wake and free surface. While the tip-struts configuration offers some improvement in efficiency, it leads to a slower wake recovery under shallow immersion. The latter is important to consider when designing a tidal array, where downstream turbines are influenced by the wake of upstream turbines. In such a case, the tip vortices generated by the open blade-tips of the quarter-struts configuration are beneficial in

improving the wake recovery rate.

For future work, this study can be extended to investigate the effects of the seafloor on the performance of the turbine. Such a study is useful for turbines operating in shallow channels, where both the effect of the free surface and seafloor may be important. Realistic inflow conditions such as a turbulent inflow or airy waves can also be prescribed to improve the faithfulness of the simulations to site-specific conditions.

5.3 Limitations of the current study

As with most engineering work, it is instructive to begin with simpler cases and gradually add complexity. Therefore, there are some limitations in the current study which will be addressed in future work. In both Chapters 3 and 4, the effect of the seafloor is ignored. When both the free surface and seafloor are considered, there may exist an optimum depth of immersion where the power coefficient is greatest. The free surface in Chapter 4 also does not include oncoming waves which may increase the unsteadiness of the power coefficient curves. In Chapter 3, the turbulent statistics used for the turbulent inflow are not site-specific as this data was not available. Using site-specific data would result in more accurate results, but the general effect of a turbulent inflow should be the same. Lastly, while the tip-struts configuration was more efficient than the quarter-struts configuration, the effect of strut placement on the structural integrity of the blades was not considered in the present analysis.

Bibliography

- Afgan, I., McNaughton, J., Rolfo, S., Apsley, D., Stallard, T., Stansby, P., 2013. Turbulent flow and loading on a tidal stream turbine by LES and RANS. *International Journal of Heat and Fluid Flow* 43, 96–108.
- Ahmadi, M., 2019. Influence of upstream turbulence on the wake characteristics of a tidal stream turbine. *Renewable Energy* 132, 989–997.
- Ahmed, U., Apsley, D., Afgan, I., Stallard, T., Stansby, P., 2017. Fluctuating loads on a tidal turbine due to velocity shear and turbulence: Comparison of CFD with field data. *Renewable Energy* 112, 235–246.
- Akin, J.E., Tezduyar, T., Ungor, M., Mittal, S., 2003. Stabilization parameters and Smagorinsky turbulence model. *Journal of Applied Mechanics* 70, 2–9. doi:[10.1115/1.1526569](https://doi.org/10.1115/1.1526569).
- Akkerman, I., Bazilevs, Y., Benson, D.J., Farthing, M.W., Kees, C.E., 2012a. Free-surface flow and fluid–object interaction modeling with emphasis on ship hydrodynamics. *Journal of Applied Mechanics* 79, 010905.
- Akkerman, I., Dunaway, J., Kvandal, J., Spinks, J., Bazilevs, Y., 2012b. Toward free-surface modeling of planing vessels: simulation of the Fridsma hull using ALE-VMS. *Computational Mechanics* 50, 719–727.
- Baba-Ahmadi, M., Tabor, G., 2009. Inlet conditions for LES using mapping and feedback control. *Computers and Fluids* 38, 1299–1311.
- Bachant, P., Wosnik, M., 2011. Experimental investigation of helical cross-flow axis hydrokinetic turbines, including effects of waves and turbulence, in: *Proceedings of the ASME-JSME-KSME 2011 Joint Fluids Engineering Conference*, pp. 1–12.
- Bachant, P., Wosnik, M., 2014. Reynolds number dependence of cross-flow turbine performance and near-wake characteristics, in: *Proceedings of the 2nd Marine Energy Technology Symposium, METS, Seattle*. pp. 1–9.
- Bachant, P., Wosnik, M., 2015. Characterising the near-wake of a cross-flow turbine. *Journal of Turbulence* 16, 392–410.

- Bachant, P., Wosnik, M., 2016. Modeling the near-wake of a vertical-axis cross-flow turbine with 2-D and 3-D RANS. *Journal of Renewable and Sustainable Energy* 8.
- Bahaj, A., Molland, A., Chaplin, J., Batten, W., 2007. Power and thrust measurements of marine current turbines under various hydrodynamic flow conditions in a cavitation tunnel and a towing tank. *Renewable Energy* 32, 407–426.
- Bai, X., Avital, E., Munjiza, A., Williams, J., 2014. Numerical simulation of a marine current turbine in free surface flow. *Renewable Energy* 63, 715–723.
- Bayram, A., Bear, C., Bear, M., Korobenko, A., 2020. Performance analysis of two vertical-axis hydrokinetic turbines using variational multiscale method. *Computers & Fluids* 200, 104432. doi:doi.org/10.1016/j.compfluid.2020.104432. available online.
- Bayram, A., Dhalwala, M., Oshkai, P., Korobenko, A., 2022. Numerical simulations of a vertical-axis hydrokinetic turbine with different blade-strut configurations under free-surface effects. *Engineering with Computers* Under review.
- Bayram, A., Korobenko, A., 2020. Variational multiscale framework for cavitating flows. *Computational Mechanics* 66, 49–67. doi:doi.org/10.1007/s00466-020-01840-2.
- Bayram, A., Korobenko, A., 2021. A numerical formulation for cavitating flows around marine propellers based on variational multiscale method. *Computational Mechanics* 68, 405–432. doi:<https://doi.org/10.1007/s00466-021-02039-9>.
- Bayram Mohamed, A., Abdulrahman, M., Guaily, A., 2022. Simplified level set method coupled to stabilised finite element flow solver for moving boundaries. *Progress in Computational Fluid Dynamics, an International Journal* 22, 1–14. doi:[10.1504/PCFD.2022.120265](https://doi.org/10.1504/PCFD.2022.120265).
- Bazilevs, Y., Calo, V.M., Cottrell, J.A., Hughes, T.J.R., Reali, A., Scovazzi, G., 2007a. Variational multiscale residual-based turbulence modeling for large eddy simulation of incompressible flows. *Computer methods in applied mechanics and engineering* 197, 173–201.
- Bazilevs, Y., Calo, V.M., Cottrell, J.A., Hughes, T.J.R., Reali, A., Scovazzi, G., 2007b. Variational multiscale residual-based turbulence modeling for large eddy simulation of incompressible flows. *Computer Methods in Applied Mechanics and Engineering* 197, 173–201.
- Bazilevs, Y., Calo, V.M., Hughes, T.J.R., Zhang, Y., 2008. Isogeometric fluid-structure interaction: theory, algorithms, and computations. *Computational mechanics* 43, 3–37.

- Bazilevs, Y., Hughes, T.J.R., 2007. Weak imposition of Dirichlet boundary conditions in fluid mechanics. *Computers & Fluids* 36, 12–26.
- Bazilevs, Y., Hughes, T.J.R., 2008. NURBS-based isogeometric analysis for the computation of flows about rotating components. *Computational Mechanics* 43, 143–150.
- Bazilevs, Y., Michler, C., Calo, V.M., Hughes, T.J.R., 2007c. Weak Dirichlet boundary conditions for wall-bounded turbulent flows. *Computer Methods in Applied Mechanics and Engineering* 196, 4853–4862.
- Benhamadouche, S., Jarrin, N., Addad, Y., Laurence, D., 2006. Synthetic turbulent inflow conditions based on a vortex method for large-eddy simulation. *Progress in Computational Fluid Dynamics* 6, 50–57.
- Blackmore, T., Myers, L., Bahaj, A., 2016. Effects of turbulence on tidal turbines: Implications to performance, blade loads, and condition monitoring. *International Journal of Marine Energy* 14, 1–26.
- Boudreau, M., Dumas, G., 2017. Comparison of the wake recovery of the axial-flow and cross-flow turbine concepts. *Journal of Wind Engineering and Industrial Aerodynamics* 165, 137–152.
- Boudreau, M., Dumas, G., 2018. Vortex dynamics in the wake of three generic types of freestream turbines. *Journal of Fluids Engineering, Transactions of the ASME* 140, 021106.
- Brooks, A.N., Hughes, T.J.R., 1982. Streamline upwind/Petrov-Galerkin formulations for convection dominated flows with particular emphasis on the incompressible Navier-Stokes equations. *Computer Methods in Applied Mechanics and Engineering* 32, 199–259.
- Brownstein, I., Kinzel, M., Dabiri, J., 2016. Performance enhancement of downstream vertical-axis wind turbines. *Journal of Renewable and Sustainable Energy* 8, 053306.
- Brownstein, I., Wei, N., Dabiri, J., 2019. Aerodynamically Interacting Vertical-Axis Wind Turbines: Performance Enhancement and Three-Dimensional Flow. *Energies* 12, 1–23.
- Bruno, L., Salvetti, M., Ricciardelli, F., 2014. Benchmark on the aerodynamics of a rectangular 5:1 cylinder: An overview after the first four years of activity. *Journal of Wind Engineering and Aerodynamics* 126, 87–106.
- Buffa, E., Jacob, J., Sagaut, P., 2021. Lattice-Boltzmann-based large-eddy simulation of high-rise building aerodynamics with inlet turbulence reconstruction. *Journal of Wind Engineering and Industrial Aerodynamics* 212, 104560.
- Celik, I.B., Ghia, U., Roache, P.J., Freitas, C.J., 2008. Procedure for estimation and reporting of uncertainty due to discretization in CFD applications. *Journal of fluids Engineering-Transactions of the ASME* 130, 078001.

- Choma, B., Carlier, C., Fur, A., Pinon, G., Germain, G., Rivoalen, E., 2020. A stochastic method to account for the ambient turbulence in Lagrangian Vortex computations. *Applied Mathematical Modelling* 88, 38–54.
- Chung, J., Hulbert, G.M., 1993. A time integration algorithm for structural dynamics with improved numerical dissipation: the generalized- α method. *Journal of Applied Mechanics* .
- Codoni, D., Johansen, C., Korobenko, A., 2022. A Streamline-Upwind Petrov–Galerkin formulation for the analysis of hypersonic flows in thermal non-equilibrium. *Computer Methods in Applied Mechanics and Engineering* 398, 115185. doi:<https://doi.org/10.1016/j.cma.2022.115185>.
- Codoni, D., Moutsanidis, G., Hsu, M.C., Bazilevs, Y., Johansen, C., Korobenko, A., 2021. Stabilized methods for high-speed compressible flows: toward hypersonic simulations. *Computational Mechanics* 67, 785–809.
- Consul, C., Willden, R., McIntosh, S., 2013. Blockage effects on the hydrodynamic performance of a marine cross-flow turbine. *Philosophical Transactions of the Royal Society A: Mathematical, Physical and Engineering Sciences* 371, 1–16.
- Dabiri, J., 2011. Potential order-of-magnitude enhancement of wind farm power density via counter-rotating vertical-axis wind turbine arrays. *Journal of Renewable and Sustainable Energy* 3, 043104.
- Dhalwala, M., Bayram, A., Oshkai, P., Korobenko, A., 2022. Performance and near-wake analysis of a vertical-axis hydrokinetic turbine under a turbulent inflow. *Ocean Engineering* 257, 111703. Available online.
- Dhamankar, N., Blaisdell, G., Lyrantzis, A., 2015. An overview of turbulent inflow boundary conditions for large eddy simulations, in: *American Institute of Aeronautics and Astronautics*, pp. 1–28.
- Ebdon, T., Allmark, M., O’Doherty, D., Mason-Jones, A., O’Doherty, T., Germain, G., Gaurier, B., 2019. The impact of turbulence and turbine operating condition on the wakes of tidal turbines. *Renewable Energy* 165.
- Elgeti, S., Sauerland, H., 2014. Deforming fluid domains within the finite element method: Five mesh-based tracking methods in comparison. *Archives of Computational Methods in Engineering* , 323–361.
- Faizan, M., Badshah, S., Badshah, M., Haider, B., 2022. Performance and wake analysis of horizontal axis tidal current turbine using Improved Delayed Detached Eddy Simulation. *Renewable Energy* 184.
- Gajardo, D., Escauriaza, C., Ingram, D., 2019. Capturing the development and interactions of wakes in tidal turbine arrays using a coupled BEM-DES model. *Ocean Engineering* 181.
- Gant, S., Stallard, T., 2008. Modelling a tidal turbine in unsteady flow, in: *International Society of Offshore and Polar Engineers*, pp. 1–7.

- Gosselin, R., Dumas, G., Boudreau, M., 2016. Parametric study of H-Darrieus vertical-axis turbines using CFD simulations. *Journal of Renewable and Sustainable Energy* 8.
- Gravemeier, V., 2006. The variational multiscale method for laminar and turbulent flow. *Archives of Computational Methods in Engineering* 13.
- Grondeau, M., Guillou, S., Poirier, J., Mercier, P., Poizot, E., Méar, Y., 2022. Studying the Wake of a Tidal Turbine with an IBM-LBM Approach Using Realistic Inflow Conditions. *Energies* 15.
- Guillaud, N., Balarac, G., Goncalvès, E., Zanette, J., 2020. Large eddy simulations on vertical axis hydrokinetic turbines - power coefficient analysis for various solidities. *Renewable Energy* 147, 473–486.
- Hezaveh, S., Bou-Zeid, E., Dabiri, J., Kinzel, M., Cortina, G., Martinelli, L., 2018. Increasing the Power Production of Vertical-Axis Wind-Turbine Farms Using Synergistic Clustering. *Boundary-Layer Meteorology* 169, 275–296.
- Hocine, A., Lacey, R., Poncet, S., 2019. Multiphase modeling of the free surface flow through a darrieus horizontal axis shallow-water turbine. *Renewable Energy* 143, 1890–1901.
- Hsu, M.C., Bazilevs, Y., Calo, V.M., Tezduyar, T.E., Hughes, T.J.R., 2010. Improving stability of stabilized and multiscale formulations in flow simulations at small time steps. *Computer Methods in Applied Mechanics and Engineering* 199, 828–840. doi:[10.1016/j.cma.2009.06.019](https://doi.org/10.1016/j.cma.2009.06.019).
- Jansen, K.E., Whiting, C.H., Hulbert, G.M., 2000. A generalized- α method for integrating the filtered navier–stokes equations with a stabilized finite element method. *Computer methods in applied mechanics and engineering* 190, 305–319.
- Jarrin, N., Benhamadouche, S., Laurence, D., Prosser, R., 2006. A synthetic-eddy-method for generating inflow conditions for large-eddy simulations. *International Journal of Heat and Fluid Flow* 27, 585–593.
- Jarrin, N., Prosser, R., Uribe, J., Benhamadouche, S., Laurence, D., 2009. Reconstruction of turbulent fluctuations for hybrid RANS/LES simulations using a synthetic-eddy method. *International Journal of Heat and Fluid Flow* 30, 435–442.
- Jin, G., Zong, Z., Jiang, Y., Zou, L., 2020. Aerodynamic analysis of side-by-side placed twin vertical-axis wind turbines. *Ocean Engineering* 209.
- Katopodes, N., 2018. *Free-Surface Flow: Computational Methods*. Elsevier.
- Kempf, A., Wysocki, S., Pettit, M., 2012. An efficient, parallel low-storage implementation of Klein’s turbulence generator for LES and DNS. *Computers and Fluids* 60, 58–60.

- Klein, M., Sadiki, A., Janicka, J., 2003. A digital filter based generation of inflow data for spatially developing direct numerical or large eddy simulations. *Journal of Computational Physics* 186, 652–665.
- Kolekar, N., Banerjee, A., 2015. Performance characterization and placement of a marine hydrokinetic turbine in a tidal channel under boundary proximity and blockage effects. *Applied Energy* 148, 121–133.
- Kraichnan, R., 1970. Diffusion by a random velocity field. *Physics of Fluids* 13, 22–31.
- Laws, N., Epps, B., 2016. Hydrokinetic energy conversion: Technology, research, and outlook. *Renewable and Sustainable Energy Reviews* 57, 1245–1259.
- Mannini, C., Marra, A., Pigolotti, L., Bartoli, G., 2017. The effects of free-stream turbulence and angle of attack on the aerodynamics of a cylinder with rectangular 5:1 cross section. *Journal of Wind Engineering and Industrial Aerodynamics* 161, 42–58.
- Marsh, P., Ranmuthugala, D., Penesis, I., Thomas, G., 2015a. Numerical investigation of the influence of blade helicity on the performance characteristics of vertical axis tidal turbines. *Renewable Energy* 81, 926–935.
- Marsh, P., Ranmuthugala, D., Penesis, I., Thomas, G., 2015b. Three-dimensional numerical simulations of straight-bladed vertical axis tidal turbines investigating power output, torque ripple and mounting forces. *Renewable Energy* 83, 67–77.
- Marsh, P., Ranmuthugala, D., Penesis, I., Thomas, G., 2015c. Three-dimensional numerical simulations of straight-bladed vertical axis tidal turbines investigating power output, torque ripple and mounting forces. *Renewable Energy* 83, 67–77.
- Marsh, P., Ranmuthugala, D., Penesis, I., Thomas, G., 2017. The influence of turbulence model and two and three-dimensional domain selection on the simulated performance characteristics of vertical axis tidal turbines. *Renewable Energy* 105, 106–116.
- McCaffrey, K., Fox-Kemper, B., Hamlington, P., Thomson, J., 2015. Characterization of turbulence anisotropy, coherence, and intermittency at a prospective tidal energy site: Observational data analysis. *Renewable Energy* 76, 441–453.
- Melikoglu, M., 2018. Current status and future of ocean energy sources: A global review. *Ocean Engineering* 148, 563–573.
- Milne, I., Day, A., Sharma, R., Flay, R., 2016. The characterisation of the hydrodynamic loads on tidal turbines due to turbulence. *Renewable and Sustainable Energy Reviews* 56, 851–864.

- Milne, I., Sharma, R., Flay, R., Bickerton, S., 2013. Characteristics of the turbulence in the flow at a tidal stream power site. *Philosophical Transactions of the Royal Society A: Mathematical, Physical and Engineering Sciences* 371, 1–14.
- Mycek, P., Gaurier, B., Germain, G., Pinon, G., Rivoalen, E., 2014a. Experimental study of the turbulence intensity effects on marine current turbines behaviour. Part I: One single turbine. *Renewable Energy* 66, 729–746.
- Mycek, P., Gaurier, B., Germain, G., Pinon, G., Rivoalen, E., 2014b. Experimental study of the turbulence intensity effects on marine current turbines behaviour. Part II: Two interacting turbines. *Renewable Energy* 68, 876–892.
- Nachtane, M., Tarfaoui, M., Goda, I., Rouway, M., 2020. A review on the technologies, design considerations and numerical models of tidal current turbines. *Renewable Energy* 157, 1274–1288.
- Nag, A., Sarkar, S., 2021. Performance analysis of Helical Savonius Hydrokinetic turbines arranged in array. *Ocean Engineering* 241.
- New Energy Corporation, 2021. New Energy Corporation. <https://www.newenergycorp.ca/>.
- Nezu, I., Nakagawa, H., 1993. *Turbulence in Open-Channel Flows*. Taylor & Francis Group.
- Nguyen, M., Balduzzi, F., Goude, A., 2021. Effect of pitch angle on power and hydrodynamics of a vertical axis turbine. *Ocean Engineering* 238.
- Osawa, Y., Kalro, V., Tezduyar, T., 1999. Multi-domain parallel computation of wake flows. *Computer Methods in Applied Mechanics and Engineering* 174, 371–391. doi:10.1016/S0045-7825(98)00305-3.
- Pelc, R., Fujit, R., 2002. Renewable energy from the ocean. *Marine Policy* 26, 471–479.
- Rezaeiha, A., Montazeri, H., Blocken, B., 2018. Towards optimal aerodynamic design of vertical axis wind turbines: Impact of solidity and number of blades. *Energy* 165, 1129–1148.
- Ricci, M., Patruno, L., de Miranda, S., Ubertini, F., 2017. Flow field around a 5:1 rectangular cylinder using LES: Influence of inflow turbulence conditions, spanwise domain size and their interaction. *Computers and Fluids* 149, 181–193.
- Riglin, J., Schleicher, W., Liu, I., Oztekin, A., 2015. Characterization of a micro-hydrokinetic turbine in close proximity to the free surface. *Ocean Engineering* 110, 270–280.
- Rogelj, J., Elzen, M., Hohne, N., Fransen, T., Fekete, H., Winkler, H., Schaeffer, R., Sha, F., Riahi, K., Meinshausen, M., 2016. Paris agreement climate proposals need a boost to keep warming well below 2°C. *Perspective* 534, 631–639.

- Saad, Y., 2003. Iterative methods for sparse linear systems. volume 82. SIAM.
- Sentchev, A., Thiébaud, M., Schmitt, F., 2020. Impact of turbulence on power production by a free-stream tidal turbine in real sea conditions. *Renewable Energy* 147, 1932–1940.
- Smirnov, A., Shi, S., Celik, I., 2001. Random flow generation technique for large eddy simulations and particle-dynamics modeling. *Journal of Fluids Engineering, Transactions of the ASME* 123, 359–371.
- Strom, B., Johnson, N., B.Polagye, 2018. Impact of Blade Mounting Structures on Cross-Flow Turbine Performance. *Journal of Sustainable and Renewable Energy* 10, 034504.
- Sun, K., Yi, Y., Zhang, J., Haider, S., Sun, S., 2021. Influence of blade numbers on start-up performance of vertical axis tidal current turbines. *Ocean Engineering* 243.
- Sun, K., Yi, Y., Zhang, J., Zhang, J., Zaidi, S., Sun, S., 2022. Influence of blade numbers on start-up performance of vertical axis tidal current turbines. *Ocean Engineering* 243, 110314.
- Tabor, G., Baba-Ahmadi, M., 2010. Inlet conditions for large eddy simulation: A review. *Computers and Fluids* 39, 553–567.
- Takizawa, K., Tezduyar, T.E., Otaguro, Y., 2018. Stabilization and discontinuity-capturing parameters for space–time flow computations with finite element and isogeometric discretizations. *Computational Mechanics* 62, 1169–1186. doi:[10.1007/s00466-018-1557-x](https://doi.org/10.1007/s00466-018-1557-x).
- Taylor, G., 1938. The spectrum of turbulence. *Philosophical Transactions of the Royal Society A: Mathematical and Physical Sciences* 164, 476–490.
- Teske, S., 2019. Achieving the Paris Climate Agreement Goals: Global and Regional 100% Renewable Energy Scenarios with Non-energy GHG Pathways for +1.5°C and +2°C. Springer.
- Tezduyar, T., Aliabadi, S., Behr, M., 1998. Enhanced-Discretization Interface-Capturing Technique (EDICT) for computation of unsteady flows with interfaces. *Computer Methods in Applied Mechanics and Engineering* 155, 235–248.
- Tezduyar, T., Sathe, S., 2003. Stabilization parameters in SUPG and PSPG formulations. *Journal of Computational and Applied Mechanics* 4, 71–88.
- Tezduyar, T.E., 2003. Computation of moving boundaries and interfaces and stabilization parameters. *International Journal for Numerical Methods in Fluids* 43, 555–575.

- Tezduyar, T.E., 2007. Finite elements in fluids: stabilized formulations and moving boundaries and interfaces. *Computers & fluids* 36, 191–206.
- Tezduyar, T.E., Ramakrishnan, S., Sathe, S., 2008a. Stabilized formulations for incompressible flows with thermal coupling. *International Journal for Numerical Methods in Fluids* 57, 1189–1209. doi:[10.1002/flid.1743](https://doi.org/10.1002/flid.1743).
- Tezduyar, T.E., Ramakrishnan, S., Sathe, S., 2008b. Stabilized formulations for incompressible flows with thermal coupling. *International Journal for Numerical Methods in Fluids* 57, 1189–1209.
- Tezduyar, T.E., Senga, M., 2007. SUPG finite element computation of inviscid supersonic flows with $YZ\beta$ shock-capturing. *Computers & fluids* 36, 147–159.
- Togneri, M., Pinon, G., Carlier, C., Choma, C., Masters, I., 2020. Comparison of synthetic turbulence approaches for blade element momentum theory prediction of tidal turbine performance and loads. *Renewable Energy* 145, 408–418.
- Veers, P., 1988. Three-Dimensional Wind Simulation. Technical Report. Sandia National Laboratories.
- Villeneuve, T., Dumas, G., 2021. Impact of some design considerations on the wake recovery of vertical-axis turbines. *Renewable Energy* 180, 1419–1438.
- Villeneuve, T., Winckelmans, G., Dumas, G., 2021. Increasing the efficiency of vertical-axis turbines through improved blade support structures. *Renewable Energy* 169, 1386–1401.
- Whelan, J., Thomson, M., Grahamland, J., Peiro, J., 2007. Modelling of free surface proximity and wave induced velocities around a horizontal axis tidal stream turbine, in: *Proceedings of the 7th European Wave and Tidal Energy Conference*, pp. 1–7.
- Widén, J., Carpman, N., Castellucci, V., Lingfor, D., Olauson, J., Remouit, F., Bergkvist, M., Grabbe, M., Waters, R., 2015. Variability assessment and forecasting of renewables: A review for solar, wind, wave and tidal resources. *Renewable and Sustainable Energy Reviews* 44, 356–375.
- Xie, Z., Castro, I., 2008. Efficient generation of inflow conditions for large eddy simulation of street-scale flows. *Flow, Turbulence, and Combustion* 81, 449–470.
- Yan, B., Li, Q., 2015. Inflow turbulence generation methods with large eddy simulation for wind effects on tall buildings. *Computers and Fluids* 116, 158–175.
- Yan, J., Deng, X., Korobenko, A., Bazilevs, Y., 2017. Free-surface flow modeling and simulation of horizontal-axis tidal-stream turbines. *Computers & Fluids* 158, 157–166. doi:[10.1016/j.compfluid.2016.06.016](https://doi.org/10.1016/j.compfluid.2016.06.016).

Zanforlin, S., 2018. Advantages of vertical axis tidal turbines set in close proximity: A comparative CFD investigation in the English Channel. *Ocean Engineering* 156.